

MULTI-DIRECTIONAL LIGHT COUPLING STRUCTURES  
FOR NANOMEMBRANE PHOTONIC  
INTEGRATION

by

TAPAS KUMAR SAHA

Presented to the Faculty of the Graduate School of  
The University of Texas at Arlington in Partial Fulfillment  
of the Requirements  
for the Degree of

DOCTOR OF PHILOSOPHY

THE UNIVERSITY OF TEXAS AT ARLINGTON

MAY 2012

Copyright © by Tapas Kumar Saha 2012

All Rights Reserved

## ACKNOWLEDGEMENTS

I pay my humble obeisances to His Divine Grace, A.C. Bhaktivedanta Swami Prabhupada, whom I have accepted as my spiritual master in my mind. He has explained me in a very nice way that, what, is the actual mission of my life. I pay my sincere gratitude to The Supreme Personality Godhead, Krishna, under whose shelter I always enjoy transcendental bliss, life after life. I pay my gratitude to Swami Ramdev from whose teachings I have learnt the art of meditation, yoga and pranayam.

I will stay indebted to my PhD Supervisor, Prof. Weidong Zhou, for his eternal mercifulness, as he has always forgiven all my limitations and mistakes, without any punishment. I am thankful to my PhD Co-advisor Prof. Mingyu Lu, under whose guidance I understood so many interesting intricacies of the beautiful subject Electromagnetic Theory. I am indebted to Prof. Robert Magnusson for being in my PhD Committee and through his breakthrough research I have understood the details of Diffraction and scattering of Light. I am grateful to Prof. Michael Vasilyev and Late Prof. Nikolai Stelmakh, who taught me very interesting phenomena of Light matter interactions in their classes. I pay my thanks to Prof. Wei Chen, from UTA Physics Department, for being in my PhD Committee Member. I am thankful to Prof. Kambiz Alavi and Saibun Tjuatja for their generosity and helpfulness in the time of need.

I am grateful to the great devotees of the very beautiful temple ISKCON Dallas, like Nityananda Prabhu, Rasraj Das, Acyuta Govinda Das, Ramasundar Das, Nityananda Chandra Das, who have enlightened me with the spiritual knowledge of Lord Krishna.

I pay my sincere gratefulness to my parents and my sweet brother. I am indebted to my friends like Steve Headland, Bhargav Nabar, Tom, Bryan, Vitthal, Parthivan Mani and Gautam Chavan.

I will stay indebted to my research group members: Dr. Deyin Zhao, Dr. Zexuan Qiang, Dr. Weiquan Yang, Dr. Yuehui Wang, Dr. Li Chen, Dr. Hongjun Yang, Rajesh Tummala, Santhad Chuwongin, Arvinder Chadha, Yichen Shuai, Laxmi Menon, Shuling Wang, Nandan and Guru for their kind support and friendly assistances.

I am indebted to all the staffs of Nanofab like Manager Nader Hozhabri, Thanh Bui, Chris Carter, Dennis Bueno, Richard K. Chambers, Richard E. Wells and Paul C. Logan.

I will stay grateful to the amazing group of staffs of the Department of Electrical Engineering, who have always stood by me in the time of need. The list includes Gail Paniuski, Ann Lewiston, Janice Moore, Bess Alvarez, Pauline Mason and Terri Earle.

Thank You very much for all of your kind support.

April 20, 2012



## ABSTRACT

# MULTI-DIRECTIONAL LIGHT COUPLING STRUCTURES FOR NANOMEMBRANE PHOTONIC INTEGRATION

Tapas Kumar Saha

The University of Texas at Arlington, 2012

Supervising Professor: Weidong Zhou

Vertical coupling of light within an in-plane nanophotonic waveguide is an essential step towards the successful future realization of CMOS compatible optical interconnects and photonic integrated circuits. This is especially important, since silicon, though being the material of choice, is an extremely poor emitter of light. Through vertical to in-plane coupling, light can be coupled through any point on the planar on chip and the position is not only confined within the edges of the silicon wafer. Compact wafer scale testing is possible with this approach, without the need for polished edge cleaving.

Another important aspect of this research is that nanomembrane technology has opened a new dimension to the 3D vertical heterogeneous integration of different optical materials on Silicon. Since silicon itself is a transparent medium in the telecom band, it cannot become a source or detector of the light. The transferred nanomembrane technology can successfully replace the conventional unreliable bonding process which also wastes too much space within the Silicon wafer. New enhanced integrated on-chip functionalities, new device physics are realizable with the aid of the nanomembrane technology.

In Chapter 2 we have presented the design of a compact high efficiency first order grating coupler with Silicon nanomembrane whose performance is extremely robust to fabrication error. Two-dimensional model simulation shows a diffractive power-up efficiency of 81% and a fibre coupling efficiency of 64%. With nanomembrane stacking, it is feasible to integrate the side-distributed Bragg reflector and bottom reflector, which can lead to the diffractive power-up efficiency and the fibre coupling efficiency of 97% and 73.5%, respectively.

In Chapter 3 we present, the design of a compact, frequency selective, efficient second-order grating coupler for normally incident light. Traditionally the high efficiency, compact grating couplers are extremely broadband (linewidth>30 nm). Through making use of transverse resonance and evanescent field coupling, the coupler designed, exhibits high frequency-selectiveness with controllable linewidths. Full-wave simulations based on finite-difference-time-domain method demonstrate Q of 2350 with a coupling efficiency of 37%.

In Chapter 4 a laser beam angle detector is designed using a second order grating coupler. The designed coupler can detect upto  $4^\circ$  to achieve fast responding on-chip detection of the laser beam steering. The range of the angle that can be determined by this method depends on the linewidth of the coupled resonance, the laser power and the detector sensitivity.

In Chapter 5 we have designed a 2D second order grating coupler which can couple surface normal incident light with high coupling efficiency contrast of 7 to 10 between the two orthogonal polarizations over a 24 nm band linewidth. The device can work in illuminated or semi-illuminated environment. The device can give information regarding the direction of the incident source and is extremely promising for fast high contrast thermal imaging.

In Chapter 6, we present the main conclusion of our research and the perspectives for future work.

## TABLE OF CONTENTS

ACKNOWLEDGEMENT .....	iii
ABSTRACT .....	v
LIST OF ILLUSTRATIONS .....	viii
LIST OF TABLES .....	xiii
Chapter	Page
1. INTRODUCTION .....	1
2. HIGH EFFICIENCY DIFFRACTIVE GRATING COUPLER BASED ON TRANSFERRED SILICON NANOMEMBRANE OVERLAY ON PHOTONIC WAVEGUIDE .....	3
3. DESIGN OF A COMPACT GRATING COUPLER WITH CONTROLLABLE LINEWIDTHS VIA TRANSVERSE RESONANCE AND EVANESCENT FIELD COUPLING .....	22
4. DESIGN OF A SECOND ORDER GRATING COUPLER FOR LASER BEAM ANGLE DETECTION .....	33
5. DESIGN OF A 2D GRATING COUPLER FOR POLARIZATION DETECTION .....	48
6. CONCLUSION AND PERSPECTIVES .....	60
APPENDIX	
A. LIST OF PUBLICATIONS .....	62
REFERENCES .....	64
BIOGRAPHICAL INFORMATION .....	69

## LIST OF ILLUSTRATIONS

Figure	Page
1 The schematic of diffraction based grating coupler (a) with deposited poly-silicon overlay and oxide buffer; (b) with transferred silicon nanomembrane (SiNM) overlay and oxide buffer; and (c) with SiNM overlay and air buffer. (d) Multi-layer optical interconnect for high density vertical integration of optical/electrical components. ....	5
2 The modified wet transfer process for the fabrication of SiNM overlay based grating coupler on the SOI waveguide. ....	6
3 Simulated coupling performance for the SiNM overlay structure shown in Fig. 1(b), with IML on top and oxide buffer layer below: (a) Wavelength dependent coupling efficiency; and (b) the effect of etch depth from the top of the silicon overlay (SiNM) layer at $\lambda = 1550\text{nm}$ . ....	9
4 The variation of power diffracting upward at $\lambda = 1550\text{nm}$ for different etch depths from the overlay top, for the diffraction based grating coupler with silicon overlay. The parameters are retained the same as published in[19-20]. ....	10
5 (a) Coupling efficiency of the diffraction based grating coupler with SiNM overlay, oxide on top and Air buffer (b) The effect of etch depth from Silicon overlay top at $\lambda = 1550\text{nm}$ . ....	11
6 Field plots of the optimized grating coupler based on SiNM overlay (a) positively detuned (b) negatively detuned. ....	13
7 Coupling efficiency for a negatively detuned diffraction based grating coupler with SiNM overlay and Air Buffer below. ....	14
8 The grating coupler with SiNM overlay and air buffer. The coupler is terminated by a side-DBR and a bottom reflector to maximize the efficiency. ....	15
9 Performance of positively detuned SiNM overlay coupler with a side-DBR and a bottom reflector: (a) Variation of the coupling efficiency with respect to the spacing doff, the distance between the coupler grating and the side-DBR; and (b) Coupling efficiency for different wavelengths. ....	16
10 Performance of negatively detuned SiNM overlay coupler with a side-DBR only: (a) Variation of the coupling efficiency with respect to the spacing doff; and (b) Coupling efficiency for different wavelengths. Notice that the bottom reflector is not incorporated in this case. ....	17

11 Variations of fiber coupling efficiencies (at wavelength $\lambda = 1550$ nm) with the coupling angles of fiber for (a) Positively detuned and (b) Negatively detuned diffractive grating couplers based on SiNM overlay with optimized parameters. Notice that the bottom reflector and Side-DBR are not incorporated in these structures.....	18
12 Device configuration. 2D Layered structure, infinitely extended in the y direction. (b) Reflection Spectra of the device, when $t_c = 0.2 \mu\text{m}$ . Simulation results by 2D FDTD and FEM are shown. ....	23
13 Steady-state field distribution within the unit cell of the device at the phase matching resonant frequency and $t_c=0.2\mu\text{m}$ , with continuous wave excitation obtained by FEM simulation. When the incident wave has amplitude 1, field amplitude of 109 is observed within the waveguide manifesting the occurrence of high Q within the waveguide. ....	25
14 (top) FDTD simulated single frequency pulse transient response showing the time-variation of the field within the waveguide of the device. $E_y^{wg}$ being the field within the center of the waveguide and (middle) $E_y^{inc}$ being the excitation field (bottom) the zoomed-in version of the incident field $E_y^{inc}$ showing sinusoidal time-variation.....	25
15 (a) Fourier Transform of the FDTD calculated field within the center of the waveguide, manifests the selectivity of Device in frequency domain, for two values of the spacing $t_c$ , between the waveguide and the grating. Larger spacing $t_c$ , yields higher Q and selectivity. (b) Variation of Q with respect to the spacing between the waveguide and the grating $t_c$ . Consideration of the extremely ideal scenario of the infinitely extended lossless in-plane periodicity yields exponential increase in Q with $t_c$ . ....	26
16 Schematic of the finite grating coupler structure with the waveguide being terminated with Quarter-Wave reflectors (QWR) laterally.....	27
17 FDTD simulated single-side Coupling efficiency within the waveguide .....	28
18 Schematic of the unidirectional finite grating coupler structure with the waveguide being terminated with Quarter-Wave reflectors (QWR) laterally .....	28
19 FDTD simulated Coupling efficiency within the waveguide.....	29
20 Schematic of the finite grating coupler structure with the waveguide being terminated with Si-Oxide Quarter-Wave reflectors (QWR) laterally .....	29
21 FDTD simulated Coupling efficiency within the waveguide for Si-Oxide QWR structure.....	30
22 Schematic of the unidirectional finite grating coupler structure with the waveguide being terminated with Si-Oxide Quarter-Wave reflectors (QWR) laterally. Here two QWRs are shown .....	30

23 FDTD simulated Coupling efficiency within the waveguide for 1 period Si-Oxide QWR structure.....	31
24 FDTD simulated Coupling efficiency within the waveguide structure, showing the effect of number of periods of the QWR for gap $t_c=0.178\mu\text{m}$ . ....	31
25 FDTD simulated field plot for $t_c=0.178\mu\text{m}$ and 2 Si-Ox QWR.....	32
26 FDTD simulated Coupling efficiency within the waveguide, with 3 period Si-Oxide QWR for gap $t_c=0.178\mu\text{m}$ . ....	32
27 A Illustration of induced beam collimation by means of a small aperture .....	35
28 Demonstration of the surface normal light coupling within a second order diffraction based grating coupler (b) The angular response of the coupled spectrum. The zero frequency denotes the resonance frequency of the coupled light spectrum. The positive and negative coupling strength values indicates the direction of the light to Port 1 and Port 2 of the coupler respectively .....	36
29 Structural modification of the grating coupler to minimize interference within the waveguide (a) the paths available to the scattered lights are (i) To the port 1 (ii) to the port 2 (iii) back reflection; the incident beam is shown in blue and the scattered light paths are shown in red (b) The structure with grating on top of the waveguide provides lesser interference than that of the grating etched within a thicker waveguide (c) The spectrum of the broadband grating reflector with the period $\Lambda$ being $1.05\mu\text{m}$ , Si filling fraction $ff=0.2$ and grating thickness $t_g=0.26\mu\text{m}$ (d) The transmitted light T in the glass substrate and coupled light C for normal incidence is shown for waveguide thickness $t_{wg}=0.26\mu\text{m}$ and $0.22\mu\text{m}$ . ....	38
30 2D FDTD simulated Design of the grating coupler to determine angle by ratio method. Si on glass implementation (a) The spectrum of the coupled and the transmitted light for normal incidence. (b) The ratio between the Port 2 and Port 1 coupled power. Variation of coupling efficiency with incident angle in (c) Port 2 and (d) Port 1 .....	39
31 2D FDTD simulated Design of the grating coupler on SOI to determine angle by ratio method. (a) The spectrum of the coupled and the transmitted light for normal incidence. (b) The ratio between the Port 2 and Port 1 coupled power. Variation of coupling efficiency with incident angle in (c) Port 2 and (d) Port 1 .....	41
32 Schematic to illustrate the detection of angle of incidence $\theta_i$ of any arbitrary Laser. The main grating is used calculate the ratio of coupled in the two waveguide ports. The support grating determines that whether the incidence angle is on the higher or in the lower side. The two gratings differs in the period only. For our design $\Lambda_s=1.05\mu\text{m}$ and $\Lambda_m=1.065\mu\text{m}$ .....	42
33 2D FDTD simulated Results of the grating coupler on glass substrate to determine angle by ratio method of any arbitrary Laser. (a) The ratio between the Port 2 and Port 1 coupled power of the main grating. The main grating period $\Lambda_m$ being $1.065\mu\text{m}$ , the support grating period $\Lambda_s=1.050\mu\text{m}$ , (b) Variation of coupling efficiency with incident angle in Port 2 for the support and main grating (c)	

The ratio between the Port 2 coupled powers of the main and support grating (d) The magnified version of the (c) indicating that when the support grating receives more power the incident angle is greater than 3 degree. ....	43
34 2D FDTD simulated Results of the grating coupler on SOI to determine angle by ratio method of any arbitrary Laser. (a) The ratio between the Port 2 and Port 1 coupled power of the main grating. The main grating period $\Lambda_m$ being 1.065 $\mu\text{m}$ , the support grating period $\Lambda_s=1.050 \mu\text{m}$ , (b) Variation of coupling efficiency with incident angle in Port 2 for the support and main grating (c) The ratio between the Port 2 coupled powers of the main and support grating (d) The magnified version of the (c) indicating that when the support grating receives more power the incident angle is greater than 3 degree. ....	44
35 2D FDTD simulated Results of the grating coupler analyzing its sensitivity to detect the angles (a) The single side coupling efficiency at surface normal incidence $\theta_i=0^\circ$ for different number of grating periods N and source width. The grating period $\Lambda$ being 1.065 $\mu\text{m}$ , (b) The normalized coupling efficiency for different number of grating periods N and source width indicating that the linewidth decreases with increase in number of gratings N (c) The ratio between the Port 2 and Port 1 coupled power for different number of grating periods N and source width indicating that the angular sensitivity increases with increase in N. The frequency being $f_0=0.645(c/a)$ (d) The ratio between the Port 2 and Port 1 coupled power for $N=21$ and source width= $16\Lambda$ , for two different frequencies. $\eta_0$ being the single side coupling efficiency for surface normal incidence $\theta_i=0^\circ$ .....	45
36 (a) The schematic of the 2D second order grating coupler to detect the polarization (b) (top) The cross-section of the 3D FDTD computational cell. Note that in the computation silicon on glass substrate is considered (Down) The top view of the 2D grating depicting the definition of polarization (c) The 3D FDTD simulated coupling efficiency within each waveguide, for surface normal incidence. (d) The ratio between of the coupled power with orthogonal polarizations .....	49
37 The variation of the ratio of the coupled power within the two adjacent waveguides for different values of polarization angles $\psi$ . The wavelength is 1.549 $\mu\text{m}$ .....	50
38 (a) The schematic cross-section of the 3D FDTD computational cell. Note that in the computation SOI is considered (b) 3D FDTD simulated coupling efficiency within each waveguide, for surface normal incidence. (c) The ratio between of the coupled power with orthogonal polarizations.....	51
39 The schematic of the 2D second order grating coupler to detect the polarization with etch stop layer in between the 2D gratings and the waveguide. ....	52
40 The schematic of the 2D second order grating coupler with thin etch stop layer, to detect the polarization (a) The cross-section of the 3D FDTD computational cell. Note that in the computation silicon on glass substrate is considered (b) The 3D FDTD simulated coupling efficiency within each waveguide, for surface normal incidence. (c) The ratio between of the coupled power with orthogonal polarizations.....	52
41 FDTD simulated results for 2D second order grating coupler with thin etch stop layer,with enhanced coupling efficiency. (a) The 3D FDTD simulated	

coupling efficiency within each waveguide, for surface normal incidence (b) The ratio between of the coupled power with orthogonal polarizations.....	53
42 (a) The schematic of the 2D second order nitide on SOI grating coupler (b) The cross-section of the device. ....	54
43 FDTD simulated results for 2D second order grating coupler with nitride on Silicon configuration. The substrate is chosen to be glass. (a) The 3D FDTD simulated coupling efficiency within each waveguide, for surface normal incidence (b) The ratio between of the coupled power with orthogonal polarizations.....	55
44 The field plot of the coupled light within the 2D grating coupler with nitride on Si configuration.....	56
45 FDTD simulated results for 2D second order grating coupler with nitride on SOI configuration (a) The 3D FDTD simulated coupling efficiency within each waveguide, for surface normal incidence (b) The ratio between of the coupled power with orthogonal polarizations .....	56
46 The schematic of the Quasi 2D second order grating coupler (a) (left) the parmeters of the transferred membrane (right) the top view of the coupler (b) The cross-section of the device. ....	57
47 The 3D FDTD simulated coupling efficiency within each waveguide, the mode being TE-like, i.e. excitation has Ey component .....	58



LIST OF TABLES

Table	Page
1 Summary of the Overlay based Diffraction Grating Coupler .....	20

## CHAPTER 1

### INTRODUCTION

#### 1.1 Research Context

Today we can hardly imagine the world without telecommunications. The internet and the computer networking have brought the whole world right at the grasp of each and everyone. The tremendous amounts of progress in the fields of telecommunications are results of fiber optic communications and optoelectronics. In order to achieve fast communications, like thousands of long distant phone calls at a time or downloading/uploading Gigabits of data within seconds needs ultrafast signal transmission, processing and reception. In this regards, the conventional electronics fail to satisfy the requirement since transistors or electrons can provide only limited bandwidths and the fast signal modulation are impossible to be realized due the large delays within the electronic interconnects.

Till now the fiber optics transports optical information from point A to B. Within the network nodes, the optical signals are then converted to electrical signals. The electrical signals are then goes through routing and processing. The electrical signal is then converted to optical signal to be retransmitted. This optoelectronic conversion limits the growth of the network. Hence an all-optical signal processing and routing is a hot topic of research today. A complete on-chip optical signal processing will pave the new path for faster telecommunication and signal processing.

#### 1.2 Nanomembrane Photonic Integration

The advent of Silicon Technology have revolutionized the whole world of electronics industry and replaced the bulky vacuum tubes based transistors to its solidstate micron scale counterpart. Due to this inspiring growth of silicon technology only sophisticated gadgets like personal computers, mobile phones, flat screen High Definition Large Televisions have become

common household tools throughout the world. However, though silicon has elevated the field of electronics to a transcendental level it is not a very merciful candidate in the fields of photonics. Being an indirect semiconductor it is a poor emitter of light and is transparent in the telecommunication wavelength of 1550 nm. Hence to make efficient light sources and detectors on Silicon platform heterogeneous integration of active materials like GaAs, InP or Ge is required. In this regard, the nanomembrane integration [1-5] on the foreign substrate has recently provided extreme boost for unprecedented on-chip compact in-plane and vertical integration.

### 1.3 Current Status and research challenges

Nanomembrane transfer and photonic integrations[1] have provided wonderful platform for realizations of optical filters [4-5], detectors [6-7], mirrors[8] on silicon. However for on-chip signal processing and routing, light has to be coupled within the nanophotonic waveguides. Therefore the coupling of the light in and out of the on-chip nanophotonic waveguide, itself is a hot topic of research today. The addition of nanomembrane integration provides an additional degree of freedom to come up with new integrated functionalities and physics to manipulate light more efficiently on Silicon.

## CHAPTER 2

### HIGH EFFICIENCY DIFFRACTIVE GRATING COUPLER BASED ON TRANSFERRED SILICON NANOMEMBRANE OVERLAY ON PHOTONIC WAVEGUIDE

#### 2.1 Introduction

The recent trend of integrating the optoelectronic devices on a single chip faces a major challenge to couple light in and out of the photonic integrated circuit. Hence the idea of channelling the light from the integrated waveguide to the external environment and vice versa has attracted much attention lately. Several works have been reported in this regard based on diffraction based one-dimensional (1D) grating couplers [9-12], 45° waveguide mirrors [13], parabolic reflectors [14], etc. Aiming to couple light to and from the nanophotonic waveguide to the single mode fiber, or to build the multilayer interconnection for three-dimensional (3D) vertical integration, the diffraction based grating structure seems to be the most compact and flexible as it can be placed in any position within the photonic integrated circuit. Such a grating coupler has the disadvantage of limited fiber coupling efficiency of 37% with air cladding on top, 44% with index matching layer (IML) on top and 53% with IML on top and optimal oxide buffer thickness, as reported in [11]. In this case, the fiber coupling efficiency is calculated considering the fiber mode to be a Gaussian profile with a beam diameter of 10.4 $\mu\text{m}$ . Apart from this limited coupling efficiency, the second disadvantage that such a grating coupler possesses is that the diffraction grating needs to be fabricated in the photonic waveguide through precisely controlled etching. In order to increase the coupling efficiency the simple grating structure has been adorned with a reflector grating and a bottom reflector [9], but the coupling efficiency still remains strongly dependent on the precision of the fabrication. Another common topology which is used for enhancement of the coupling efficiency is the slanted grating structure [15-17]. The slanted grating structure permits the field distribution to be centered within the waveguide, which

improves the mode transition from the grating to the non-grating region and thus reduces the scattering loss at the boundary. Though the theoretical efficiency of such a structure is very high at 69.8% with only 10 grating periods as reported in [15-16], the measured results in [17] and [18] are vastly different from the computed values since the fabrication of such a structure is very complex and needs high precision control in both slant angle and the etching depth. To date, the highest coupling efficiency that has been reported for straight etched grating in the optical waveguide is based on the poly-silicon overlay based grating coupler structure [19-20]. Though high coupling efficiencies of 66% theoretical and 55% experimental have been demonstrated with such a structure, precise control of etching into the silicon waveguide partially, remains necessary for its implementation [12]. Even in the most optimized structures with non-uniform grating the theoretical variation of about 5% in fiber coupling efficiency (at  $\lambda = 1550$  nm) for an etch depth error of 10 nm has been reported in [12] and a variation of about 28% in fiber coupling efficiency for an etch depth error of 20 nm has been reported in [20].

We proposed and investigated a design to diffract light by means of a grating coupler based on single crystalline silicon nanomembrane (SiNM) overlay. The nanomembrane overlay can be patterned independently and transferred onto the photonic waveguide by means of the SiNM wet transfer and stacking process [2-4]. Such crystalline semiconductor nanomembranes offer unprecedented opportunities for unique electronic and photonic devices for vertically stacked high density photonic/electronic integration. In [20], it has been demonstrated that further improvement in fiber coupling efficiency can be obtained by using non-uniform gratings in order to better match the diffracted field profile to that of the Gaussian fiber mode. Since the rate of etching is strongly dependent on tooth width, the precise control of the etch depth in the waveguide is extremely difficult, in such non-uniform structures. The SiNM, being an etch-through structure, can find a good solution to this problem.

## 2.2 The grating coupler based on SiNM overlay

### 2.2.1 Device structure and the SiNM overlay transfer

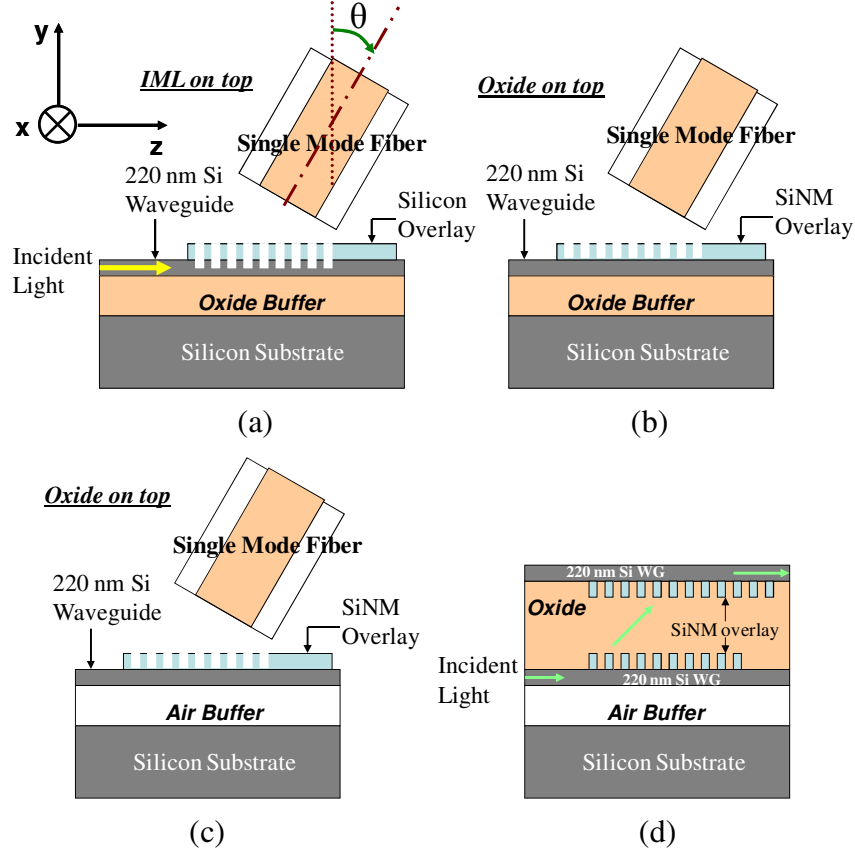


Figure 1 The schematic of diffraction based grating coupler (a) with deposited poly-silicon overlay and oxide buffer; (b) with transferred silicon nanomembrane (SiNM) overlay and oxide buffer; and (c) with SiNM overlay and air buffer. (d) Multi-layer optical interconnect for high density vertical integration of optical/electrical components.

For the sake of comparison the conventional grating coupler based on the deposited poly-silicon overlay is shown in Figure 1(a), where the precise etching into the top silicon overlay and the bottom silicon waveguide layer is essential for maximum coupling efficiency [20]. On the other hand, the proposed grating coupler based on the transferred SiNM overlay, as shown in Figure 1(b) has a much relaxed etching depth requirement.

The wet transfer process of the SiNM overlay on the silicon on insulator (SOI) waveguide has been illustrated in Figure 2. The patterning of a SiNM, its transfer and stacking on a new structure

have been elaborately discussed in [4], based on the modified transfer process developed earlier by Ma and co-workers [2]. The starting material includes two SOI wafers with device layer thickness optimized independently for the waveguide layer (e.g. 220 nm) and overlay grating

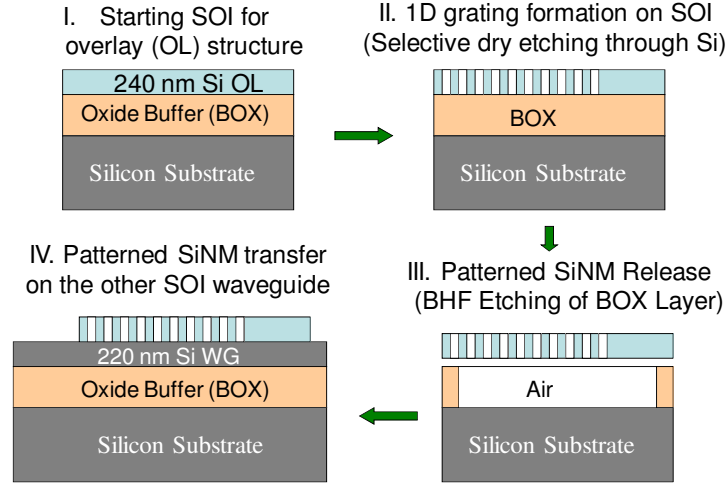


Figure 2 The modified wet transfer process for the fabrication of SiNM overlay based grating coupler on the SOI waveguide.

layer (e.g. 240 nm). The starting SOI wafer for grating overlay (Figure 2(a)) is patterned with a complete etch-through process based on the selective dry etching of the silicon layer (Figure 2(b)). The patterned nanomembrane (grating overlay) is subsequently released from the original hosting SOI substrate by immersing the patterned SOI sample in aqueous diluted HF solution for several hours to etch away the BOX layer selectively (Figure 2(c)). Finally the released grating overlay layer (SiNM) is transferred on to the second SOI wafer with optical waveguide pre-defined on the Si device layer (Figure 2(d)).

The most significant advantage of such a nanomembrane type overlay is that the performance of such a device is not sensitive to the fabrication error in the etch depth of the grating structure, since the silicon membrane is being etched through completely in the vertical direction. Another significant advantage of the SiNM overlay is that the grating coupler can be terminated by a side-DBR (also known as reflector grating, see Figure 8) to enhance the coupling efficiency by preventing the transmission loss of the optical power through the SOI waveguide.

This could not have been possible by a simple grating structure [9]. In [9], the authors have reported that it is necessary to design a reflector grating with the same etch depth as the coupler grating since the spacing between the two gratings plays a significant role in the device performance. On the other hand, the structure based on SiNM does not have such a constriction as no etching is actually done in the coupler section, hence a reflector grating with complete etch through the optical waveguide is feasible, which, in turn, not only ensures higher reflectance of the reflector grating but also the device remains much less sensitive to the spacing between the two gratings. This will be discussed further in more detail in the following sections. The device in Figure 1(c) has an air buffer instead of an oxide buffer as the isolation between the optical waveguide and the silicon substrate. Such a device can be implemented by selectively etching the buffer oxide of the SOI waveguide with the buffered HF treatment as described earlier. Based on this structure, an implementation of the multilayer optical interconnects for high density vertical integration is shown in Figure 1(d).

### *2.2.2. SiNM overlay based grating coupler performance and the effect of oxide/air as buffer layer*

The device has been simulated using CAvity Modelling FRamework (CAMFR) [21-22] , which is a two-dimensional fully vectorial solver based on eigenmode expansion, with perfectly matched layer (PML) boundary conditions. The CAMFR solver has been used extensively and successfully for the design and experimental demonstration of high performance grating structures [10, 12, 19-20]. Simulations were also carried out based on experimental results reported in [19], to ensure the accuracy of the simulation settings carried out here. The CAMFR solver is primarily used for the calculation of the diffraction efficiency, which is the ratio of the diffracted power in the superstrate (IML or oxide) to the power of the incident mode within the SOI waveguide. The transverse electric (TE) polarization, i.e. the electric field is parallel to the grating, is assumed and the target wavelength is 1550 nm. The refractive indices used in the computation were as follows: for silicon 3.476, SiO<sub>2</sub> (oxide) 1.444, IML 1.46 and air 1.0.

The device shown in Figure 1(b) consists of a SOI waveguide structure with a 220 nm thick optical waveguide and a much larger width (i.e. 12 $\mu$ m), which allows the successful 2D



treatment of the device for its design analysis. As explained in [12], because of the large width of the waveguide it is a very good approximation to write the field  $E_x(x, y)$  as  $E_x(x)E_x(y)$ .

The fiber coupling efficiency is calculated [4] by using the overlap integral,

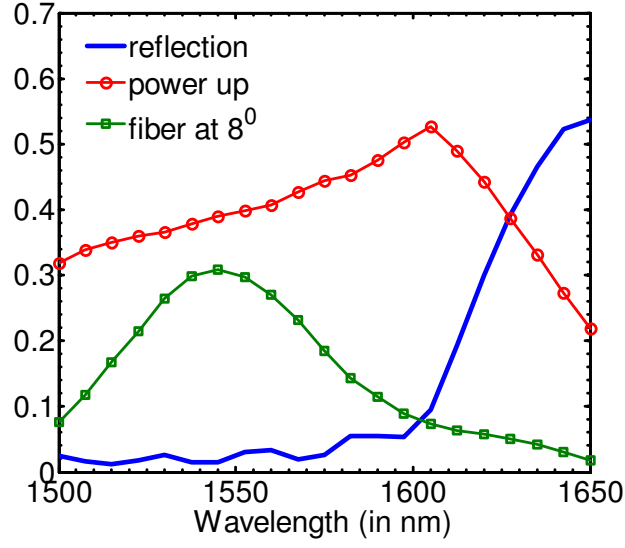
$$\eta = \left| \int \vec{E} \times \vec{H}_{fib}^* \cdot d\vec{S} \right|^2 \quad (1)$$

where  $\vec{E}$  is the electric field vector of the diffracted light in the IML/oxide cladding and  $\vec{H}_{fib}$  is the magnetic field of the fiber waveguide mode, which is also normalized in power.  $d\vec{S}$  lies along the surface normal of an integration pad in the air cladding which spans the complete grating coupler strength. Neglecting the smaller field components and the beam divergence in the lateral direction, equation (1) can be further simplified to [12, 23],

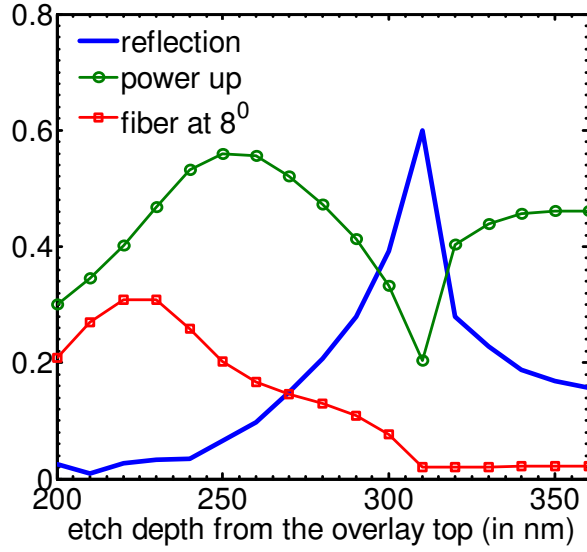
$$\eta = \left| \iint E(x)E(y = y_0, z) A e^{-\frac{(x-x_0)^2 + (z \cos \theta - z_0)^2}{\omega_0^2}} e^{(jn \frac{2\pi}{\lambda} z \sin \theta)} dx dz \right|^2 \quad (2)$$

where constant A represents the normalization of the Gaussian beam. For the position of the fiber  $y_0$  is considered to be  $1.5\mu\text{m}$  as the height of the fiber above the buffer layer.  $\theta$  is the angle of the fiber as shown in Figure 1 and  $\cos\theta$  is considered to be 1 for  $\theta \leq 16^\circ$ , which reduces the equation to the approximation that has been used in [12]. With this approximation the computation results agree very well with previously published results in [9-11, 20].

The waveguide is isolated from the silicon substrate by means of a buffer oxide layer of  $1\mu\text{m}$  to prevent leakage of light into the silicon substrate. The top of the grating is covered with either IML ( $n = 1.46$ ) or silicon dioxide ( $n = 1.444$ ) and in both the cases the simulation results vary negligibly, since the refractive index difference between the oxide and IML is only 0.016. The index matching fluid is generally applied in the case of fiber coupling to avoid the reflections at the fiber facets, whereas in the case of the high density 3D vertical integration the IML can be successfully replaced by the oxide. One important point is that equation (2) is valid for both straight cleaved or angle cleaved fiber if IML/oxide (i.e.  $n = 1.46/1.44$ ) is used as the upper



(a)



(b)

Figure 3 Simulated coupling performance for the SiNM overlay structure shown in Fig. 1(b), with IML on top and oxide buffer layer below: (a) Wavelength dependent coupling efficiency; and (b) the effect of etch depth from the top of the silicon overlay (SiNM) layer at  $\lambda = 1550\text{nm}$ .

cladding layer. But if the upper cladding is considered to be air (i.e.  $n = 1$ ), then equation (2) is only valid for straight cleaved fiber. As explained in [4], the  $x$ -dependent term in equation (2) is

considered to be 0.97 for the 12 $\mu\text{m}$  wide strip waveguide. The optimal value of  $z_0$  is dependent on the grating period and the wavelength and it has been optimized in the calculation, which provides the highest coupling efficiency  $\eta$  for the given wavelength.

Figure 3(a) shows the coupling efficiency of the grating coupler based on the SiNM overlay and oxide buffer. The grating period is 560 nm with a filling factor of 50%, the SiNM overlay layer height is 220 nm, the number of the grating periods is 20 and the oxide buffer layer thickness is 1 $\mu\text{m}$ . At the wavelength of 1550 nm the simulation shows that only 40% of the power is diffracted upwards and 31% is coupled to the fiber. In the actual simulation model, no fiber has been used and the coupling efficiency is calculated using the overlap integral with a Gaussian profile with a beam diameter of 10.4 $\mu\text{m}$ , as done in previous papers [9-12, 20].

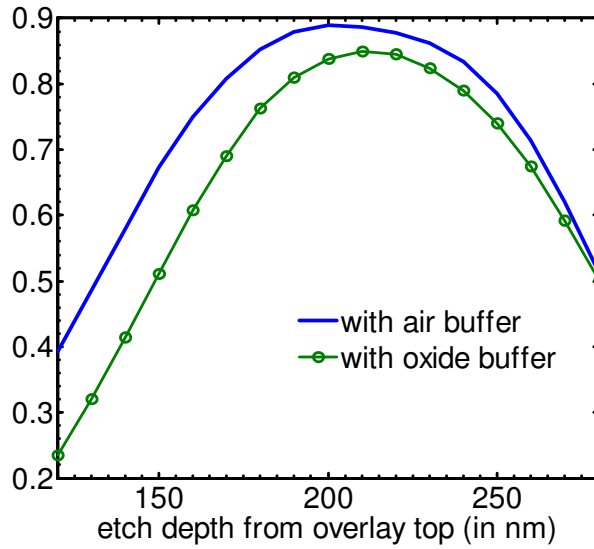
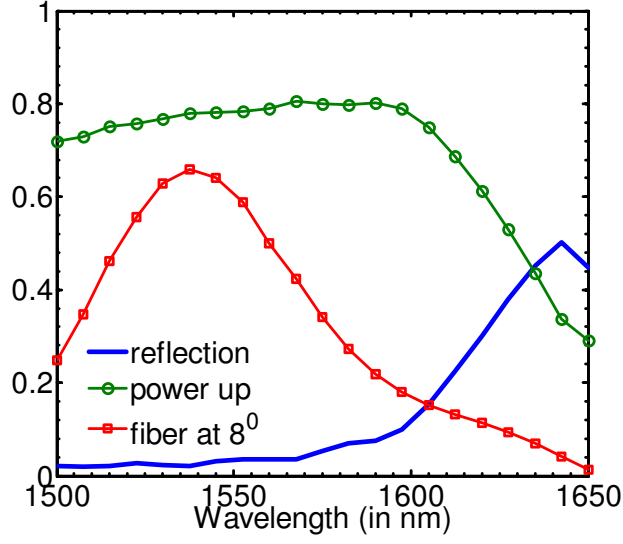
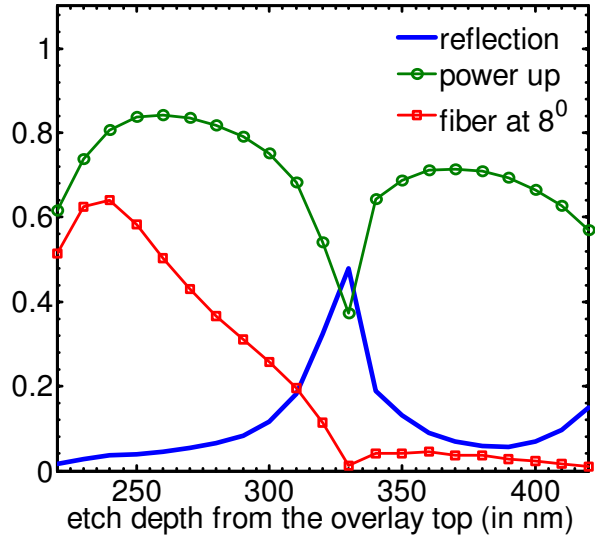


Figure 4 The variation of power diffracting upward at  $\lambda = 1550\text{nm}$  for different etch depths from the overlay top, for the diffraction based grating coupler with silicon overlay. The parameters are retained the same as published in[19-20].



(a)



(b)

Figure 5 (a) Coupling efficiency of the diffraction based grating coupler with SiNM overlay, oxide on top and Air buffer (b) The effect of etch depth from Silicon overlay top at  $\lambda = 1550\text{nm}$ .

The fiber has been kept slightly tilted from the vertical axis at an angle of  $8^\circ$  to prevent second order reflection and the coupling from the fiber to the waveguide and vice versa is considered to be the same, due to reciprocity. Figure 3(b) provides a clearer picture of the impact etch depth on the diffraction based grating coupler. For the SiNM overlay based grating coupling

structure (i.e. with an etching depth of 220 nm only on the top SiNM layer), the power-up efficiency is 40%, which is 15% lower than the over-etched conventional overlay structure, with an optimal etch depth of 250 nm (30 nm over-etching in the optical waveguide layer). This clearly signifies the fact that the etching depth into the SOI waveguide plays a very important role in increasing the efficiency of the coupling of light from the waveguide to the fiber or to the upper layer grating coupler based waveguide in the case of 3D vertical integration. However, the overlay structure can provide close to 100% power-up efficiency with the incorporation of DBRs, due to the flexible fabrication process associated with the SiNM transfer and stacking, in addition to the advantages discussed earlier in section 2.2.1.

To get a further insight into the poly-Si overlay based grating coupler, the device of Figure 1(a), which is published in [19-20], was studied further. The diffraction properties of such a grating structure can be further modified if the oxide buffer is replaced by air. This is illustrated in Figure 4. By selectively etching away the bottom oxide buffer layer, the power diffracted upwards is always higher for etch depths less than 270 nm. The grating structural parameters are kept the same as in [19-20] i.e. the grating period of 610 nm, the Si overlay layer thickness of 150 nm and the buffer layer thickness of 2  $\mu\text{m}$ . By increasing the index difference between the photonic waveguide and the isolation buffer, the field is directed much more away from the buffer and hence much more power is diffracted upwards in such a device structure.

So keeping this oxide effect in mind, the grating coupler based on the SiNM overlay is being designed as shown in Figure 1(c) and the coupling result for such a structure is shown in Figure 5(a). With a grating period of 560 nm, 50% filling factor, number of grating periods 20, overlay thickness of 220 nm, 78% of the power is diffracted up and 62% of the power is coupled into the fiber, tilted at an angle of  $8^\circ$  with respect to the surface-normal direction. The variation of the coupled power, for a 1550 nm wavelength, with etching depth from the overlay top is shown in figure 5(b). The device in this case is designed with optimum parameters with grating period 560 nm, 50% filling factor, Si overlay thickness 240 nm and air buffer thickness 1.1  $\mu\text{m}$ . The air buffer thickness plays an important role since power coupled up reaches its maximum when the power,

which is diffracted downwards towards the substrate, reflects from the substrate and interferes with the upward travelling wave constructively. From Figure 5(b) it is to be noted that with the etch depth of 240 nm, i.e. when no controlled etching in the optical waveguide is required, 81% of the power is diffracted up and 64% of the power is coupled to the fiber. The maximum diffracted power is 84.3% for an etch depth of 260 nm from the overlay top, which is only a few percentage higher than the case of nanomembrane type overlay.

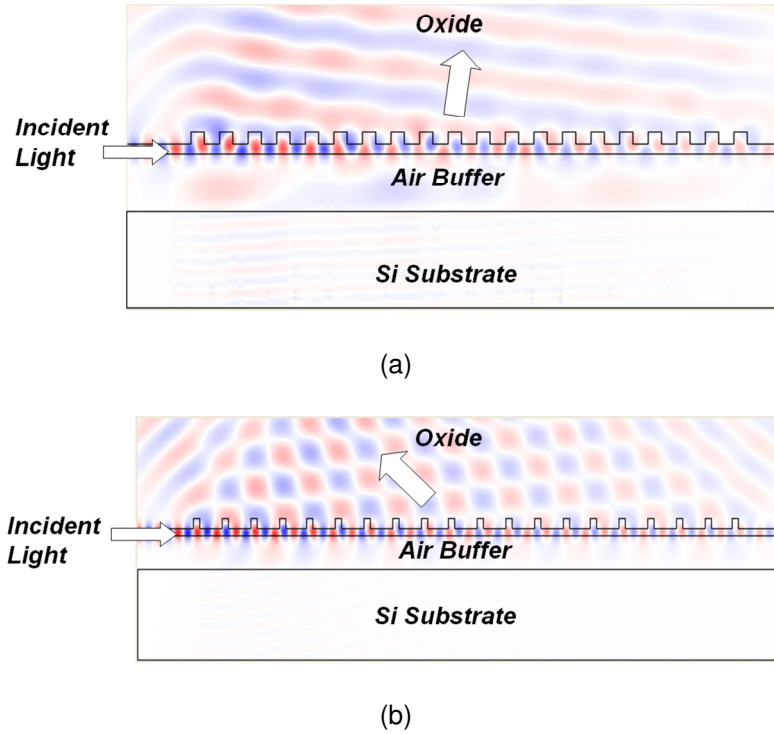


Figure 6 Field plots of the optimized grating coupler based on SiNM overlay (a) positively detuned (b) negatively detuned.

### 2.2.3. Positively/negatively detuned grating coupler based on SiNM overlay

In all the previously mentioned devices the light which is diffracted up takes the path in the same direction, inclined by a certain angle, in which the light was being incident in the waveguide. This is the case for the positively detuned grating coupler and, as shown in Figure 1(a), the fiber is tilted by a positive  $\theta$  angle with respect to the vertical axis. The field plot of such a device is shown in Figure 6(a).

In contrast, when the light is diffracted up in the opposite direction with respect to the direction of incidence, the device is said to be negatively detuned, as shown in Figure 6(b) the field propagation direction. Such a device performance based on SiNM overlay is shown in Figure 7. With a grating period of 790 nm, SiNM overlay height of 240 nm, 20 periods of grating, 25%

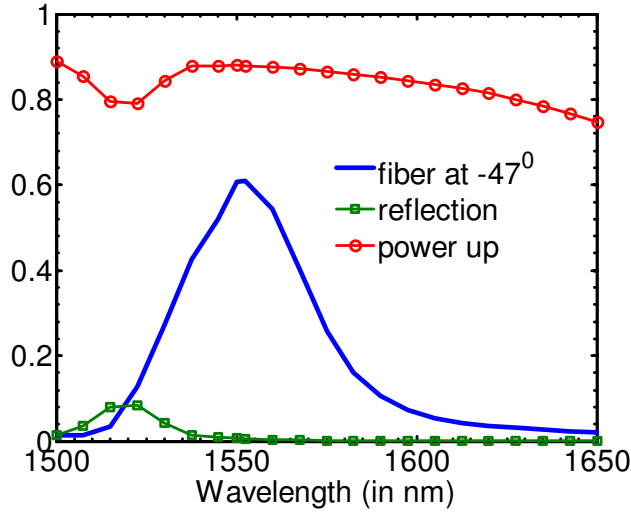


Figure 7 Coupling efficiency for a negatively detuned diffraction based grating coupler with SiNM overlay and Air Buffer below.

filling factor and air buffer thickness of  $0.8\mu\text{m}$  the device has been optimized to diffract 88% powerup and only 2% power is lost into the substrate. One major concern for such a device is that the maximum fiber coupling efficiency is only 61%, when the fiber is held at  $-47^\circ$  with respect to the vertical. The possible reason for this anomaly is that the field diffracted up has a large beam width and there is a large mismatch between the diffracted field profile and the Gaussian field profile of the optical fiber. In order to emphasize this point, the field plot for the negatively detuned grating coupler is shown in Figure 6(b). Due to the principle of reciprocity, such a device can find excellent application for the realization of compact multilayer optical interconnects in the high density 3D vertical integration. This is because, considering the symmetry of the multilayer optical interconnect, as shown in Figure 1(d), it can be inferred that the amount of power diffracted up from the bottom waveguide should be able to couple to the top waveguide completely and vice versa.

#### 2.2.4. The incorporation of side-DBR and the bottom reflector

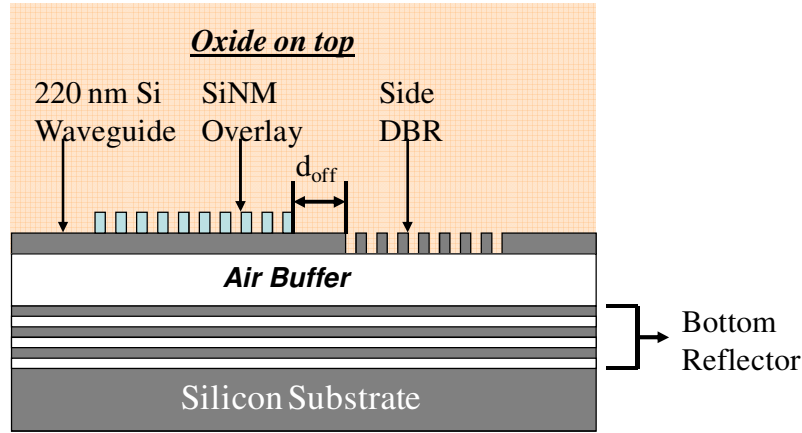


Figure 8 The grating coupler with SiNM overlay and air buffer. The coupler is terminated by a side-DBR and a bottom reflector to maximize the efficiency.

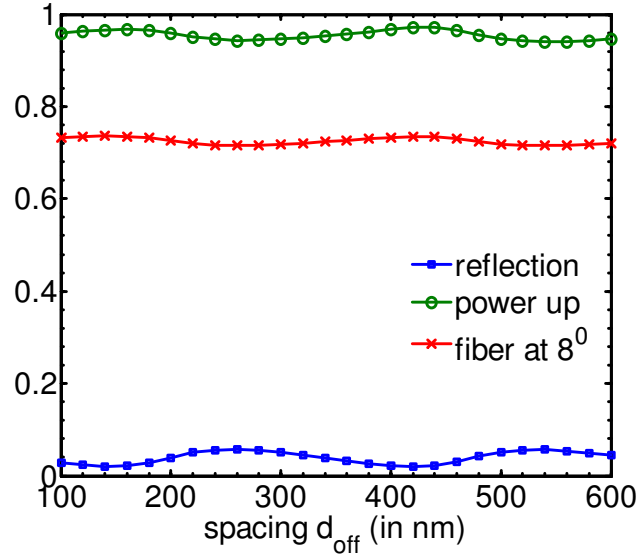
In order to further increase the coupling efficiency, the SiNM overlay based grating coupler is terminated by the side-DBR (also referred to as reflector grating in [9]) and bottom reflector. The bottom reflector can be realized by a thin layer of gold mirror [10] or DBR [9], to avoid the power loss in the silicon substrate. In this paper the bottom reflector is realized by 3 periods Si/air DBR and the side-DBR is realized by a 10 period Si/oxide DBR as shown in Figure 8. Si/oxide was chosen as the side-DBR instead of Si/Air, since through CAMFR simulation it is observed that within the 220 nm optical waveguide, higher reflectivity is obtained with a Si/oxide DBR due to lesser scattering in the interface.

Two optimized SiNM based grating couplers (i.e. positively and negatively detuned), with a side-DBR and a bottom reflector are simulated for the purpose of analysis. As discussed earlier, two significant advantages of the SiNM based overlay structure are noticeable, over the previously designed structures [9]. First, the grating coupler based on the SiNM overlay is much less sensitive to the distance between the coupler grating and the side-DBR  $d_{off}$ , which is evident in Figure 9(a) and Figure 10(a). The reason is that in such a membrane type overlay based grating structure, the waveguide transmitted power through the SiNM overlay section (i.e.

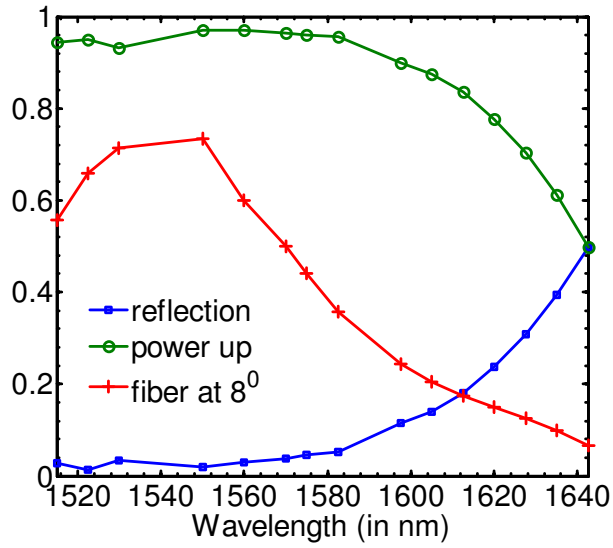


in plane transmission loss) is very low compared with the power which is being diffracted up.

Figure 9(a) is

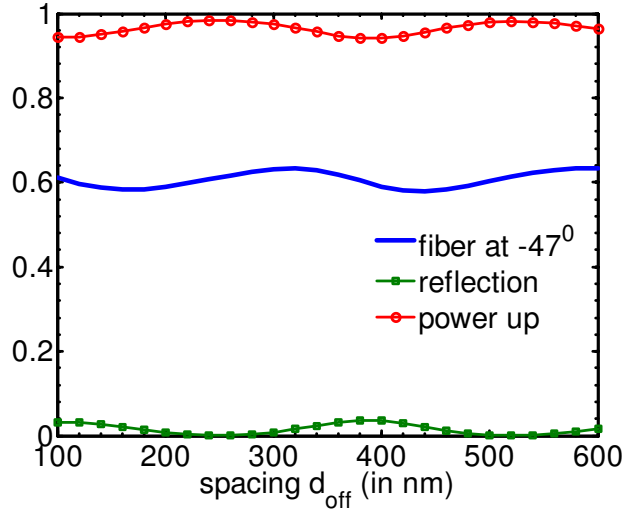


(a)

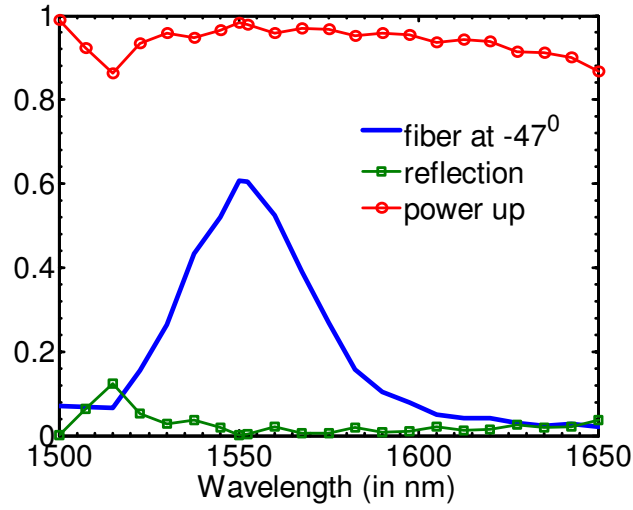


(b)

Figure 9 Performance of positively detuned SiNM overlay coupler with a side-DBR and a bottom reflector: (a) Variation of the coupling efficiency with respect to the spacing  $d_{off}$ , the distance between the coupler grating and the side-DBR; and (b) Coupling efficiency for different wavelengths.



(a)

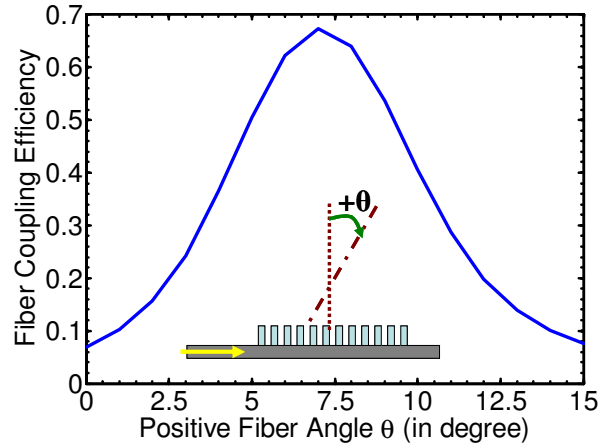


(b)

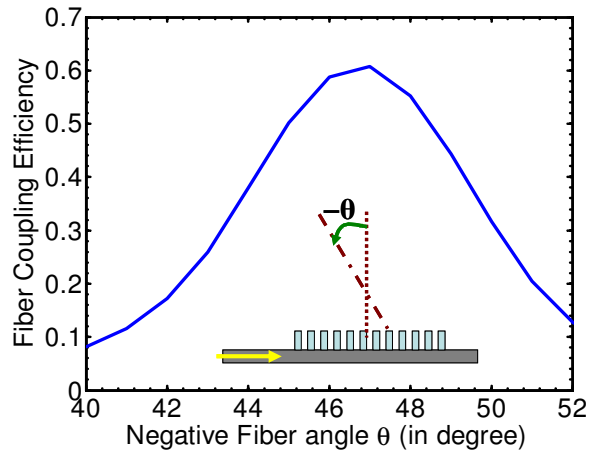
Figure 10 Performance of negatively detuned SiNM overlay coupler with a side-DBR only: (a) Variation of the coupling efficiency with respect to the spacing  $d_{\text{off}}$ ; and (b) Coupling efficiency for different wavelengths. Notice that the bottom reflector is not incorporated in this case.

the simulation result for the positively detuned grating coupler at 1550 nm wavelength, with the side-DBR and bottom reflector. The maximum occurs for  $d_{\text{off}}$  of 420 nm, where 97% of the power is diffracted up and 73.5% of the power is coupled to the fiber tilted at  $8^\circ$ . The minimum occurs for  $d_{\text{off}}$  of 540 nm, where 94% power is diffracted up and 71.6% of the power is coupled to the fiber.

Figure 9(b) shows the coupling efficiency of the positively detuned coupler with respect to the wavelength. Again, the power-up efficiency varies little over a wide simulated spectral range, from 1520 to 1580 nm.



(a)



(b)

Figure 11 Variations of fiber coupling efficiencies (at wavelength  $\lambda = 1550$  nm) with the coupling angles of fiber for (a) Positively detuned and (b) Negatively detuned diffractive grating couplers based on SiNM overlay with optimized parameters. Notice that the bottom reflector and Side-DBR are not incorporated in these structures.

For a negatively detuned structure there is an added advantage that only 2% of the power is actually lost in the substrate and hence no bottom reflector is needed in this case. Figure 10(a) shows the simulation result of the negatively detuned grating coupler with 10 periods side-

DBR only. In this case the maximum power coupled up is 98% for  $d_{\text{off}}$  of 240 nm, and the minimum is 94% for  $d_{\text{off}}$  of 400 nm. The maximum fiber coupled power is 63.5% for  $d_{\text{off}} = 580$  nm and the minimum is 58% for  $d_{\text{off}} = 440$  nm. Figure 10(b) shows the coupling efficiency for the negatively detuned grating coupler with respect to the wavelength. Hence, though incorporation of the side-DBR in the negatively detuned grating structure increases the power up diffraction efficiency by 10%, the fiber coupling efficiency remains practically unchanged. The possible reason for this anomaly is the large mismatch in the field profile between the reflected wave from the side-DBR and the Gaussian field profile of the optical fiber. While the positively detuned grating structure can be used for both fiber coupling and multilayer interconnection, the negative detuned structure may find immense application in the area of compact multilayer optical interconnections in photonic integrated circuits.

#### *2.2.5. Salient features of diffractive grating coupler based on SiNM overlay*

The fiber coupling efficiency of the designed grating coupler is dependent on the angle of the fiber which is evident from equation (2). Figure 11 shows the variation of the fiber coupling efficiency for positively and negatively detuned grating couplers based on SiNM overlay without any side-DBR and bottom reflector. For the positively detuned structure (Figure 11(a)), the coupling efficiency is highest with 67.3% at  $+7^\circ$  angle of fiber. For the negatively detuned counterpart (Figure 11(b)), the coupling efficiency reaches the peak for  $-47^\circ$  angle of fiber with an efficiency of 61%.

1D grating based devices are generally polarization sensitive, with very large polarization-dependent losses (PDLs). The devices designed here with SiNM overlay work very well for the TE polarization. In the case of transverse magnetic (TM) polarization, the optimization parameters changes vastly due to the difference in the effective index between the fundamental TE and TM modes as referred to in [19]. The fiber coupling efficiency for the TE Mode is much higher than for the TM mode because the grating coupler diffracts up the two modes at two different angles. In [4] it has been reported that for a simple grating structure with non-uniform grating, optimized for the TE mode, has a fiber coupling efficiency 21 dB lower for TM

polarization. Our calculation shows that the geometry which has been optimized for the positively detuned grating coupler has resulted in a negatively detuned structure for TM polarization and vice versa, which makes it evident that the designed grating coupler will be extremely sensitive to the polarization of the light. On the other hand, polarization insensitive coupling [24] with very small PDLs is feasible with two-dimensional grating structures or two-dimensional photonic crystal structures [4-5, 24].

Table 1 Summary of the Overlay based Diffraction Grating Coupler.

Grating coupler structure	The medium on top	The buffer material	Total power up (%)	fiber coupling (%)	fiber angle (degree)
Poly-silicon overlay based [19-20] (Figure 1(a))	IML	Oxide	84	66	10
SiNM overlay based (Figure 1(b))	IML	Oxide	40	31	8
SiNM overlay based (Figure 1(c))	Oxide	Air	78	62	8
SiNM overlay based with optimized parameters (Figure 1(c))	Oxide	Air	81	64	8
Negatively detuned SiNM overlay with optimized parameters (Figure 1(c))	Oxide	Air	88	61	-47
Positively detuned SiNM overlay with optimized parameters, side-DBR and bottom reflector (Figure 8)	Oxide	Air	97	73.5	8
Negatively detuned SiNM overlay based grating coupler with optimized parameters and side-DBR only (Figure 8)	Oxide	Air	98	61	-47

#### 2.2.6. Summary

The performance of the grating couplers, designed in this paper, has been summarized in Table 1. With optimized design parameters, record-high coupling efficiencies can be achieved, in the proposed SiNM structure, with 98% power-up coupling efficiency for the negatively detuned grating structure with side-DBR only. At the same time, close to 74% fiber coupling efficiency is

achieved in the positively detuned SiNM overlay grating structures with side-DBR and bottom reflectors.

### 2.3. Conclusion

In summary, a new type of diffraction based grating coupler with SiNM has been presented which does not require any kind of precisely controlled etching depth into the optical waveguide layer. The device is extremely flexible with a high coupling efficiency and promises to find immense application in fiber to nanophotonic waveguide coupling and in multilayer optical interconnections for vertically stacked high density photonic/electronic integration. Using the 2D model 78% power diffracted up and 62% power coupled to the fiber have been calculated. The negatively detuned counterpart promises to diffract 88% power up, which can be used for the design of a compact multilayer optical interconnect. Nearly 100% of the power-up efficiency has been achieved theoretically, when the side-DBR and the bottom reflector are added to the structure. The device structure is much less sensitive to the spacing between the side-DBR or reflector grating and the coupler grating than the previously reported devices.

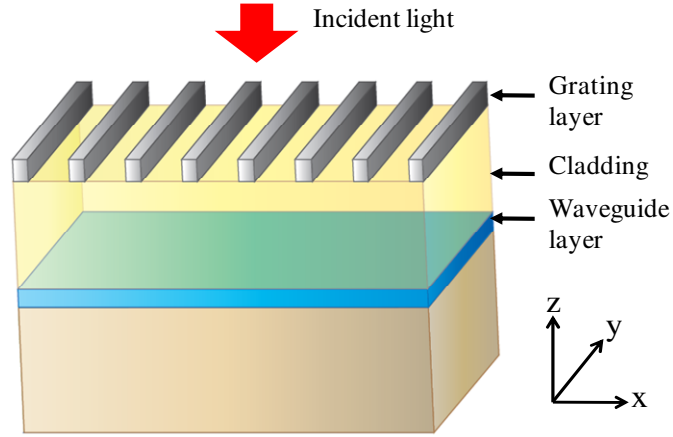
## CHAPTER 3

### DESIGN OF A COMPACT GRATING COUPLER WITH CONTROLLABLE LINEWIDTHS VIA TRANSVERSE RESONANCE AND EVANESCENT FIELD COUPLING

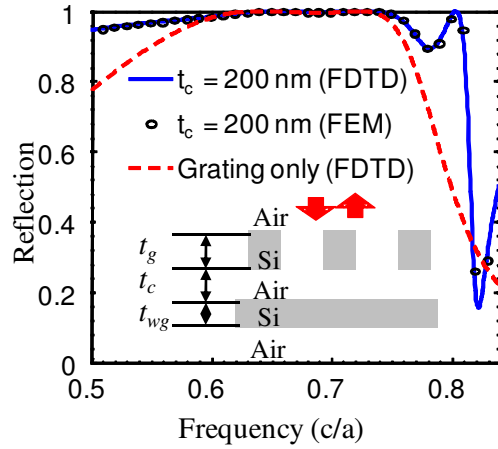
#### 3.1 Introduction

Coupling of free-space incident light within wavelength scale sized waveguide is extremely important for practical realization of photonic integrated circuit and optoelectronic devices. Compact grating-based couplers have been studied extensively [9, 12] to couple the obliquely-incident light through first order diffraction. However, such strong grating couplers being broadband, efficient and compact can be useful for realizations of light coupling from fiber to integrated chips. On the other hand, narrow-band compact couplers are extremely important for frequency selective devices like photodetectors, modulators, sensors and non-linear devices, WDM[25], and 3D vertical integration of on chip photonic applications. To some extent the narrowband coupling can be achieved by the weak grating but the device size becomes extremely large ( $> 100 \mu\text{m}$ ) to get a reasonable coupling efficiency. Another important design aspect to be noticed, in the above mentioned first-order diffraction based grating couplers, is that in all the cases the fiber is placed either obliquely or near-vertically to avoid the second-order bragg reflection. Testing and packaging with a tilted fiber in a grating coupler or with adapted fiber facets[26] is challenging. In conventional first order grating couplers the efficiency reduces drastically when the fiber is held from oblique to vertical. The reverse is worse when light is being incident vertically from fiber to the first-order grating coupler. The coupling scheme with fiber held vertically is more attractive since it facilitates dense integration, and requires much lesser space volume for wafer scale testing. In order to achieve the vertical coupling several possible approaches are being reported like parabolic reflectors [14], incorporation of side reflectors and bottom DBRs[9], incorporation of an extra slit within the waveguide[27] or the slanted grating

structure [15-17]. However all the methods are extremely complex to fabricate and the experimental results reported are far apart from its theoretical value. In this section, we present the controlling



(a)



(b)

Figure 12 Device configuration. 2D Layered structure, infinitely extended in the y direction. (b) Reflection Spectra of the device, when  $t_c = 0.2 \mu\text{m}$ . Simulation results by 2D FDTD and FEM are shown.

of the selectivity of the surface normal grating coupler, without sacrificing its compactness, by means of transverse resonance [28] and evanescent coupling. The second-order Bragg reflection is avoided by designing the second order diffraction based grating coupler (in this case the



grating periods are larger than the first order counterpart), which facilitates the surface normal vertical coupling.

### 3.2 The design of the compact grating coupler with controllable linewidths

#### *3.2.1 Transverse Resonance and Evanescent Coupling*

The device configuration is shown schematically in Figure 12(a), is composed of a 1D Silicon-Air sub-wavelength grating (SWG) [29]. This is a guided mode or fano resonance [28-31] based broadband reflector grating. The broadband reflector grating is followed by a lower index intermediate air ( $n_{\text{air}}=1.0$ ) cladding layer, a Si ( $n_{\text{Si}}=3.48$ ) planar waveguide and a air substrate. The device structure is infinitely extended in the y direction. For the structure considered here, both grating and waveguide layers are assumed to be Si, with refractive index of  $n_g=n_{\text{wg}}=n_{\text{Si}}=3.48$ . The low index of the grating is air. The cladding and the substrate layers are also assumed to be air, with index  $n_c=n_s=1$ . The grating period is  $\Lambda=1.05 \mu\text{m}$ , and the grating filling fraction  $ff=0.2$ . The grating thickness is  $t_g=260 \text{ nm}$ . The waveguide thickness is  $t_{\text{wg}}=220 \text{ nm}$ . The cladding layer thickness (i.e. the separation between the top grating SWG layer and the bottom waveguide layer) is  $t_c$ .

Shown in Figure 12(b) are the simulated reflection spectra for TE polarization (i.e. electric field parallel to the grating in y-direction), for the top SWG based broadband reflector, without and with the bottom Si planar waveguide structure. The simulations are based on 2D finite-difference time-domain (FDTD) technique and finite-element method (FEM). The reflection (>99%) frequency band spans from 0.65 to 0.737 (c/a), where c is speed of light in vacuum and  $a=1.00 \mu\text{m}$ . Within the reflection band, the surface-normal incident light is completely reflected, even if  $t_c$  is very small.

When the vertical incident light hits the top grating structure, a series of Floquet modes are generated, according to Floquet-Bloch Theorem. In order to couple the vertical incident light into the in-plane planar waveguide, phase matching conditions have to be satisfied between the higher order Floquet modes and the in-plane waveguide modes. This phase matching condition

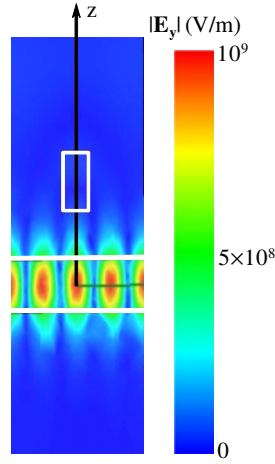


Figure 13 Steady-state field distribution within the unit cell of the device at the phase matching resonant frequency and  $t_c=0.2\mu\text{m}$ , with continuous wave excitation obtained by FEM simulation. When the incident wave has amplitude 1, field amplitude of  $10^9$  is observed within the waveguide manifesting the occurrence of high Q within the waveguide.

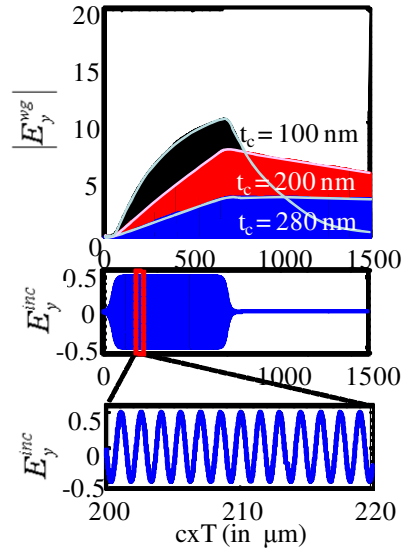
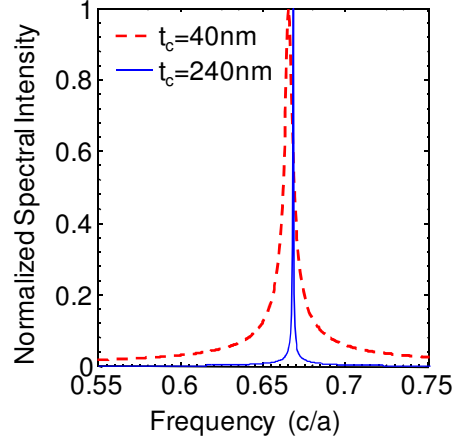


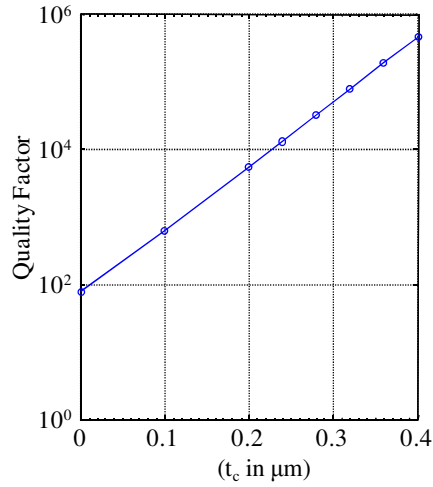
Figure 14 (top) FDTD simulated single frequency pulse transient response showing the time-variation of the field within the waveguide of the device.  $E_y^{wg}$  being the field within the center of the waveguide and (middle)  $E_y^{inc}$  being the excitation field (bottom) the zoomed-in version of the incident field  $E_y^{inc}$  showing sinusoidal time-variation

causes the transverse resonance and the field plot for the resonance is shown Figure 13. The occurrence of high Q of 5386 for  $t_c=0.2\mu\text{m}$ , within the waveguide results in huge field build up of  $10^9$  for an unit magnitude field excitation, shown by the FEM simulation. With the proper

waveguide dispersion engineering the transverse resonance frequency  $f_0^*$ , is designed within the reflection band of the grating so that light can be evanescently coupled to the waveguide.



(a)



(b)

Figure 15 (a) Fourier Transform of the FDTD calculated field within the center of the waveguide, manifests the selectivity of Device in frequency domain, for two values of the spacing  $t_c$ , between the waveguide and the grating. Larger spacing  $t_c$ , yields higher Q and selectivity. (b) Variation of Q with respect to the spacing between the waveguide and the grating  $t_c$ . Consideration of the extremely ideal scenario of the infinitely extended lossless in-plane periodicity yields exponential increase in Q with  $t_c$ .

FDTD simulation results in Figure 14 show the transient response of the device. The field build up within the center of the waveguide is evident when the device is excited by the resonant frequency pulse (at frequency  $f_0^*$ ).

As the coupling distance  $t_c$  between the waveguide and the grating increases the energy build up within the waveguide takes much longer time and it takes much more time to decay when the pulse is switched off. This shows that with the increase in  $t_c$  the power coupling efficiency within the waveguide decays but the quality factor  $Q$  within the waveguide increases. This stronger transverse resonance with increase in  $t_c$  can be physically explained that as the  $t_c$  increases the scattering due to the top grating decreases and the photon lifetime within the waveguide increases.

Theoretically speaking, its quality factor has no upper limit with the growth of  $t_c$ . In practical scenario, however the  $Q$  will be limited by the in-plane losses. A set of the Fourier transform of the fields within the center of the waveguide are shown in

Figure 15(a). The  $Q$  is 173 for  $t_c=40$  nm and it increases to 13,145 for  $t_c=240$  nm. A comprehensive evaluation of the exponential increase of  $Q$  with  $t_c$  is shown in Figure 15(b).

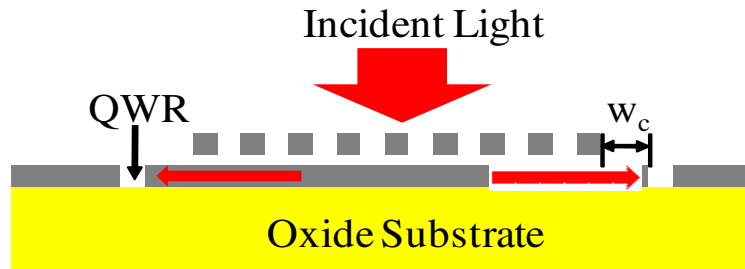


Figure 16 Schematic of the finite grating coupler structure with the waveguide being terminated with Quarter-Wave reflectors (QWR) laterally

### 3.2.2 The semi infinitely periodic device design with Si-Air QWR

We use this transverse resonance within a finite grating coupler, which is terminated by a lateral quarter wave reflector (QWR) to control the linewidth of the coupled light. The schematic of the device is shown in Figure 16 with 31 periods of grating, the source size at the top is 26

periods and the spacing between the grating and the QWR,  $w_c$  is  $2\mu\text{m}$ . The substrate is replaced by oxide which only slightly red-shifts the transverse resonance frequency  $f_0^*$ . Figure 17 shows

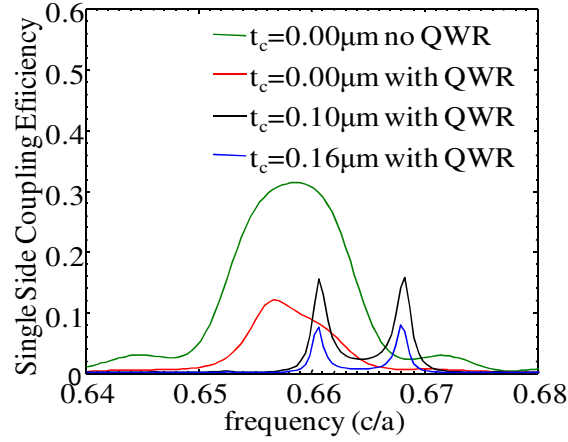


Figure 17 FDTD simulated single-side Coupling efficiency within the waveguide

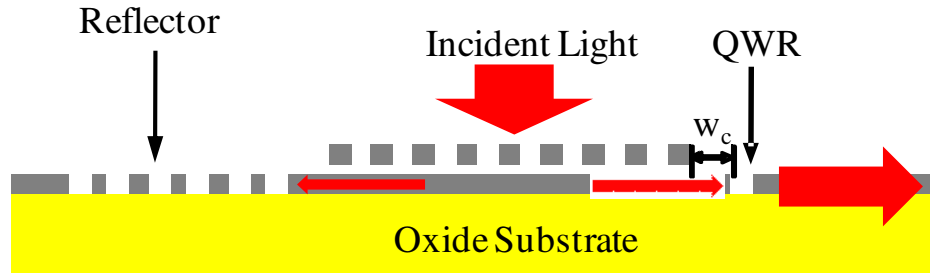


Figure 18 Schematic of the unidirectional finite grating coupler structure with the waveguide being terminated with Quarter-Wave reflectors (QWR) laterally

2D FDTD simulated coupling efficiency within one side of the waveguide. The occurrences of two resonances with identical coupling efficiencies and linewidths at frequencies  $0.6606 \text{ c/a}$  ( $\lambda_{01}=1.514\mu\text{m}$ ) and  $0.668 \text{ c/a}$  ( $\lambda_{02}=1.497\mu\text{m}$ ) for  $t_c \neq 0$ , is due to lateral movement of the light between the two lateral QWRs. All the waveguide lateral resonances within the broadband of the reflection grating are coupled via evanescently coupling. With no QWR and  $t_c=0\mu\text{m}$  the coupling efficiency at  $0.6586 \text{ c/a}$  is 31.3% and linewidth  $\Delta\lambda=26\text{nm}$  and with QWR and  $t_c=0\mu\text{m}$  the coupling efficiency at  $0.6566 \text{ c/a}$  is 12.07% and  $\Delta\lambda=18.5\text{nm}$ . For  $t_c \neq 0$ , the coupling efficiencies are 15.7%, 8% and  $\Delta\lambda=3.35\text{nm}$  ( $Q=447$ ),  $2.5\text{nm}$  ( $Q=620$ ) for  $t_c=0.1$  and  $0.16 \mu\text{m}$  respectively.

Figure 18 shows the schematic of the unidirectional vertical coupler. Figure 19 shows the device performance. The Q being 540 and 830 and coupling efficiency being 22% and 14% for  $t_c=0.10\mu\text{m}$  and  $0.16\mu\text{m}$  respectively.

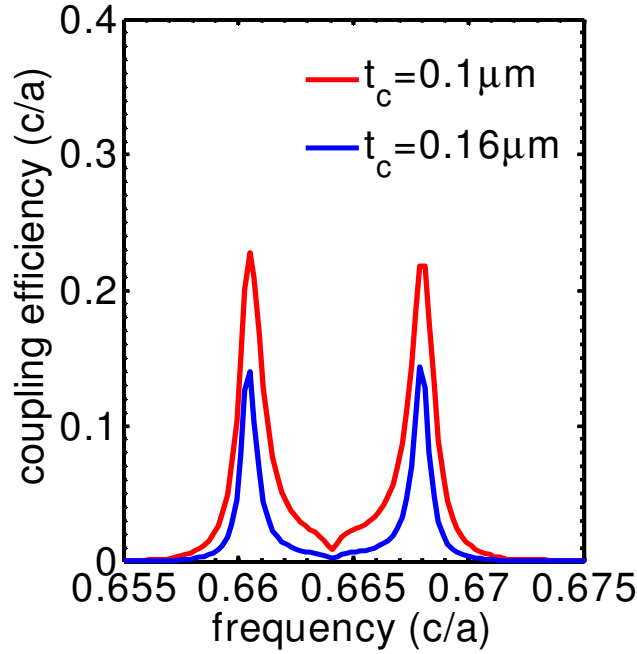


Figure 19 FDTD simulated Coupling efficiency within the waveguide

### 3.2.3 The semi infinitely periodic device design with Si-Oxide QWR

This section presents the results with above mentioned vertical coupler, however the Si-Air Quarter-Wave reflectors (QWRs) are being changed to Si-Oxide QWRs. The schematic representation of the device structure is shown in Figure 20.

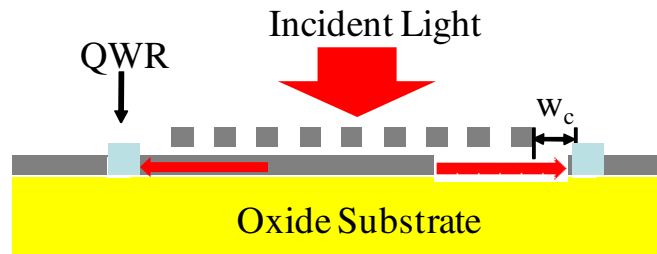


Figure 20 Schematic of the finite grating coupler structure with the waveguide being terminated with Si-Oxide Quarter-Wave reflectors (QWR) laterally

The light coupling performance is shown in Figure 21, the coupling efficiency being 20% and 10% and Q being 500 and 580 for  $t_c=0.13\mu\text{m}$  and  $0.178\mu\text{m}$  respectively.

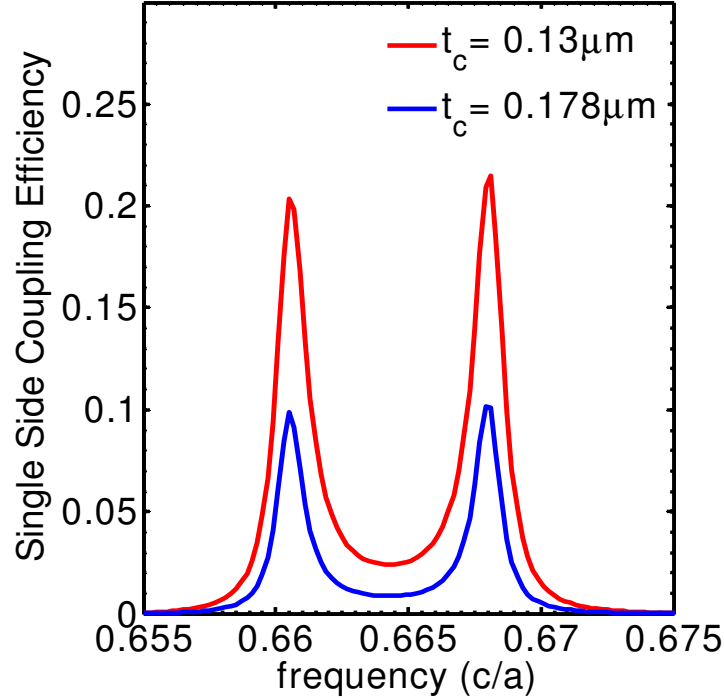


Figure 21 FDTD simulated Coupling efficiency within the waveguide for Si-Oxide QWR structure

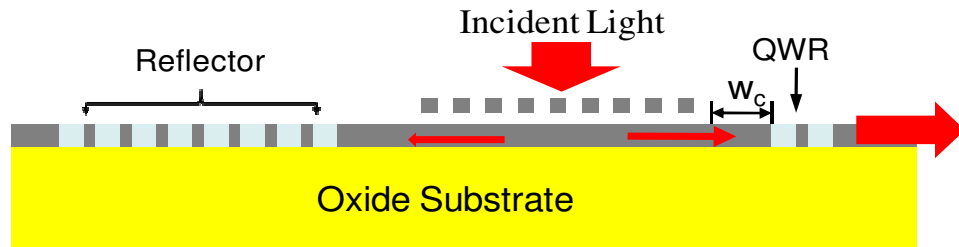


Figure 22 Schematic of the unidirectional finite grating coupler structure with the waveguide being terminated with Si-Oxide Quarter-Wave reflectors (QWR) laterally. Here two QWRs are shown

Figure 22 illustrates the schematic of a unidirectional narrow band vertical coupler, terminated in one side by reflector and the other side by two Si-Oxide QWRs. The performance of such a High Q vertical with one period Si-Oxide QWR is shown in Figure 23. The coupling efficiency being 50% with  $Q=800$  and 30% with  $Q=1040$  for  $t_c=0.13\mu\text{m}$  and  $0.178\mu\text{m}$ . The effect of change of number of QWR within the waveguide is shown in Figure 24. With  $t_c$  equals to

0.178 $\mu\text{m}$ , the coupling efficiency being 30% with  $Q=1040$  and 37% with  $Q=2350$  for 1 period and 2 periods of QWR respectively. The increase of coupling efficiency is due to the critical coupling.

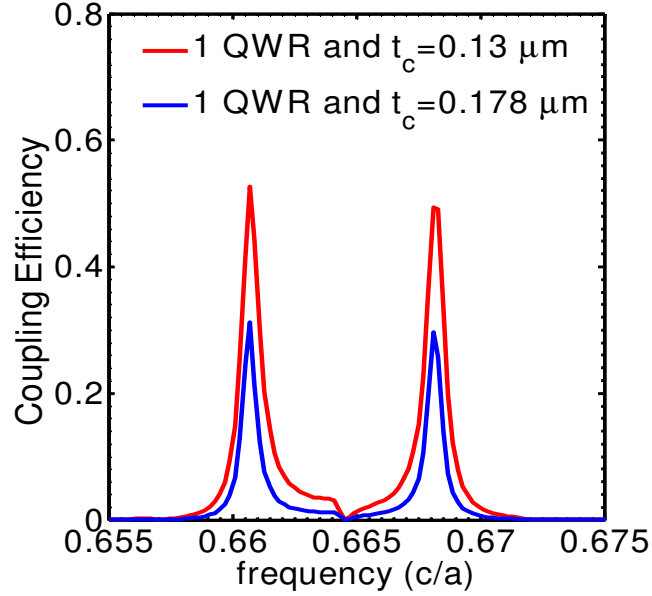


Figure 23 FDTD simulated Coupling efficiency within the waveguide for 1 period Si-Oxide QWR structure

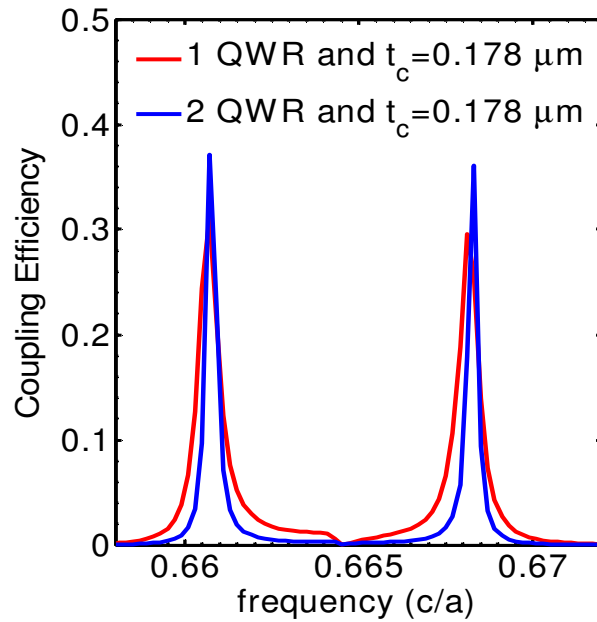


Figure 24 FDTD simulated Coupling efficiency within the waveguide structure, showing the effect of number of periods of the QWR for gap  $t_c=0.178\mu\text{m}$ .



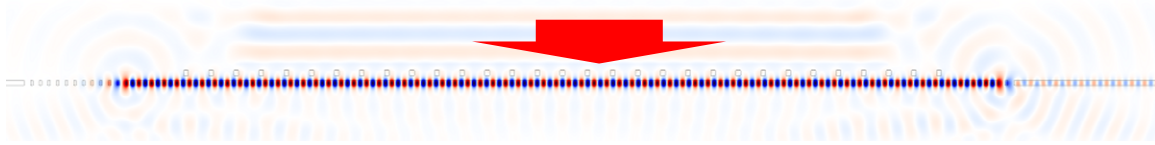


Figure 25 FDTD simulated field plot for  $t_c=0.178\mu\text{m}$  and 2 Si-Ox QWR

The field plot of the unidirectional coupler with gap  $t_c=0.178\mu\text{m}$  and 2 QWR are shown in Figure 25. The coupling efficiency being 37% and  $Q=2350$  at frequency  $0.66\text{ c/a}$ . Further investigation with 3 Si-Ox QWR shows the coupling efficiency of 25% at a  $Q$  of 3400 as illustrated in Figure 26.

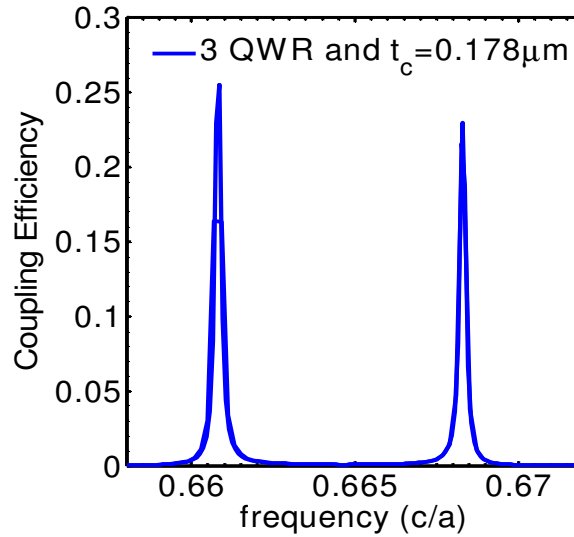


Figure 26 FDTD simulated Coupling efficiency within the waveguide, with 3 period Si-Ox QWR for gap  $t_c=0.178\mu\text{m}$ .

### 3.3. Conclusion

We report here the design of a compact, efficient second-order grating coupler for normally incident light. Through making use of transverse resonance and evanescent field coupling, the coupler designed, exhibits high frequency-selectiveness with controllable linewidths. Full-wave simulations based on finite-difference-time-domain method demonstrate unidirectional highly selective light coupling with efficiency of 37% ,  $Q=2350$  at a frequency of  $0.66\text{ c/a}$ .

## CHAPTER 4

### DESIGN OF A SECOND ORDER GRATING COUPLER FOR LASER BEAM ANGLE DETECTION

#### 4.1 Introduction

Tracking a Laser beam and determining its direction finds innumerable applications. Mechanical laser beam detection [32-35] techniques provides broad range of angle detection but the requirement of expensive high precision rotating stages increases the device complexity and are not fast enough for high speed applications. Non-contact angle measurement is extremely important for several important applications like to monitor the angle of a mirror in star tracking telescope in the field of astrometry [36-37], x-ray interferometry and testing equivalence principle using rotating masses[38].

For the purpose of precise beam alignment and detection of the incident laser beam quadrant photodiodes(QPD) have been used extensively in the field of military and lidars applications[39], chemical and biochemical microsystems[40], microscopy, optical tweezers, telescopes[37], satellite communications, laser tracking and ranging systems[41-42], coordinate measuring machines[32-33, 35], robot vision[35], real time gauge measurement[43] and high resolution angle metrology[36, 44].

Other approaches like angle measurement by injection detection in a laser diode[45] and dual focus Fresnel lens[46] are also employed but they all can detect very small angle variations like 3 mrad or 0.2 degree only and the dual Fresnel lens suffers from the spot shape degradation in higher angles. Position sensing detection is performed by lateral-effect photodiodes (LEP)[47] but its performance is limited since it is much noisier than Quadrant photodiodes.

Optical beam steering devices are extremely important for their wide range of applications in optical interconnects, optical switches, laser printers, optical scanners, optical

memory, projection systems and data conversion systems. A variety of methods have been reported by means of microelectromechanical[48], electro-optic effects[49], phased waveguide arrays[50-51]. Free space optical interconnects based on laser beam steering holds the key to replace the electrical interconnects in near future.

In pursuit of incorporating multifunctionality within the semiconductor laser itself, fast beam steering has been reported by several methods like twin stripe injection lasing[52-53], controlled profile current injection[54] and artificial band edge within composite photonic crystal structures[55]. All the above mentioned references only highlight the significance of a fast, compact, on-chip laser beam angle detector. Artificial periodic structures are by nature [56-57] highly sensitive to the wavelength, which may be used for detection of the direction of the laser beam.

In this paper we provide the complete design rule to realize a grating coupler based laser beam angle detector avoiding minimum interferences within the guiding layer. The polarization of operation is TE mode but with the same design principles holds for TM polarization as well. To our knowledge, we have for the first time designed a fast, on-chip angle detection scheme, capable measuring upto  $4^\circ$  by means of second order grating coupler. The design can be extended to larger angles depending on the laser power and the detector sensitivity.

Apart from this the device has some significant advantages over the existing Quadrant photodiode (QPD). Measurements by quadrant photodiode fails to give correct results when there is fluctuations in incident beam intensity due to the laser source or atmospheric turbulences[37]. However, due to the use of extremely small aperture (around  $30\mu\text{m}$ ) in our grating coupler based angle detector, the probability of considerable intensity fluctuation within the small beam spot is extremely low.

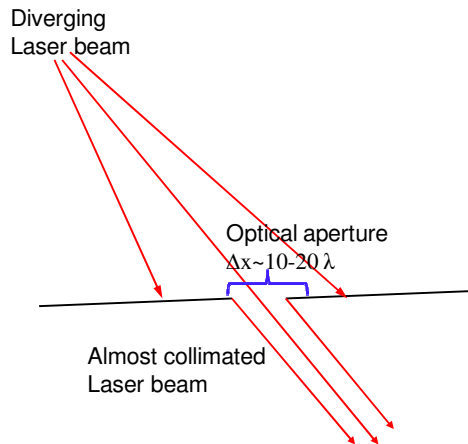


Figure 27 A Illustration of induced beam collimation by means of a small aperture

Any laser beam, though highly directional in nature, they are not highly collimated (beam divergence is much higher than 1 degree). So another advantage of having a small aperture in the vicinity of the grating region is that, the small portion of the emerging light beam can be considered to be highly collimated as illustrated in Figure 27. This also eliminates the use of an objective lens, which is a mandatory off-chip component used for finding the laser beam angle by quadrant photodiodes and lateral-effect photodiode. With the existing standard micro-fabrication techniques integration of any micro lens with proper alignment on the face of the QPD is a challenging proposition.

The sensitivity of the quadrant photodiode increases with decrease in beam spot size[41], but since the quadrant photodiode has a transition region (typically  $30\mu\text{m}$ ) separating the four detectors, the beam spot cannot be decreased arbitrarily as it may result in either beam getting undetected completely or erroneously due to low reception efficiency. On the other hand for a second order grating coupler the sensitivity can be enhanced by increasing the aperture size and the number of periods of the grating.

#### 4.2 Challenges to detect the laser Beam by a grating Coupler

The spectrum of a surface normally incident light within a second order grating coupler is shown in Figure 28(a). When the direction of the light is changed from the normal incidence to the oblique

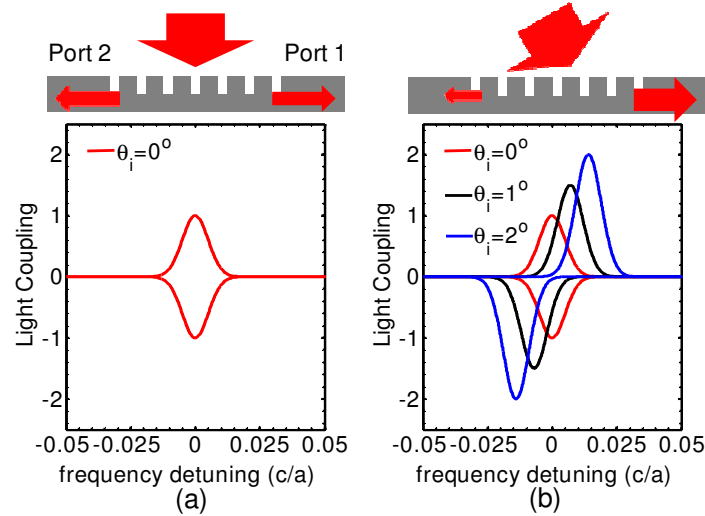


Figure 28 Demonstration of the surface normal light coupling within a second order diffraction based grating coupler (b) The angular response of the coupled spectrum. The zero frequency denotes the resonance frequency of the coupled light spectrum. The positive and negative coupling strength values indicates the direction of the light to Port 1 and Port 2 of the coupler respectively

incidence the resonance starts shifting in two opposite ways as shown in Figure 28(b). So at a particular frequency if we observe the ratio of the power between the two ports we can estimate the angle of incidence of the light. Generally after 8 degree the resonances are so much far away from each other (this depends on the linewidth of the coupled resonance) that one port almost receives no light and the measurement of the angle of incidence of the light by ratio method no longer works. This is the region where the first-order grating couplers [12] work.

So the incident angle of the laser beam can be found by two ways

- (i) *Multiple grating Methods*: Series of gratings are designed each one is optimized to couple the maximum power for a specific angle of incidence.

Practical Considerations:

(a) Interferences within the interfaces can be tolerated as the angle is not determined by the ratios between the ports but based on the maximum absolute power coupled within a port.

(b) As the coupled spectrum of the grating couplers are generally very sensitive to the angle of incidence of the light, the grating periods are only few nanometers different from each other hence demands ultra-high precision in terms of fabrication, or this method is only good for coarse estimation of incident angle of the laser beam.

(c) Apart from this, since each grating element give estimate of only one angle lots of gratings are needed to measure a wider range of angles, so this approach does not promises to provide a very compact device solution.

(ii) *Single grating method:* In this method the ratio of the coupled light power between the two ports are used to determine the incident angles of the laser beam. This method provides a more compact solution and can estimate a certain range of incident angle centered at zero degree. The central angle is zero degree because, with higher angles the spectrum of the coupled resonance are far away from each other, as described earlier.

Practical Considerations:

(a) This structure cannot tolerate any sort of interferences within the nanophotonic waveguide and a smooth monotonic spectrum of the coupled light is required. This is especially true within the port where lesser light power couples, as if small amount of light from different paths overwhelms the actual coupled power then the monotonic increase or decrease of the ratio of the power between the two ports will be hampered.

(b) A coupler with no interference involves broadband reflectors which makes the fabrication issues precise and challenging.

(c) Since a single grating coupler can estimate upto  $\pm(4-6)$  degrees (depends on the linewidth of the spectrum of the coupled light, laser power, detector sensitivity) it's a much more compact approach.

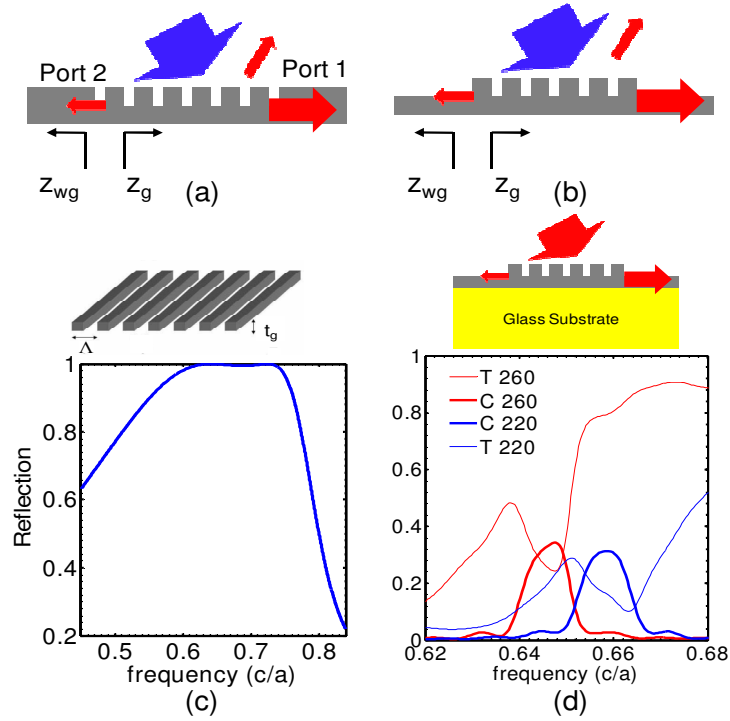


Figure 29 Structural modification of the grating coupler to minimize interference within the waveguide (a) the paths available to the scattered lights are (i) To the port 1 (ii) to the port 2 (iii) back reflection; the incident beam is shown in blue and the scattered light paths are shown in red (b) The structure with grating on top of the waveguide provides lesser interference than that of the grating etched within a thicker waveguide (c) The spectrum of the broadband grating reflector with the period  $\Lambda$  being  $1.05 \mu\text{m}$ , Si filling fraction  $ff=0.2$  and grating thickness  $t_g=0.26\mu\text{m}$  (d) The transmitted light T in the glass substrate and coupled light C for normal incidence is shown for waveguide thickness  $t_{wg}=0.26 \mu\text{m}$  and  $0.22 \mu\text{m}$ . The period  $\Lambda$  being  $1.04 \mu\text{m}$ , Si filling fraction  $ff=0.17$  and grating thickness  $t_g=0.26\mu\text{m}$ , the number of grating periods  $N=31$ , the size of the gaussian source beam  $26\Lambda$  with Gaussian beam diameter  $=26*0.9*\Lambda$  and index of the oxide substrate  $n_{ox}=1.48$

#### 4.3 Grating Coupler Design

Since the interference within the waveguide plays a very crucial issue in the design we have illustrated the required modifications of the grating couplers in Figure 29. Figure 29(a) shows that the scattered light can take only three paths and they are in the waveguides Port 1, Port 2 and back reflection with zero transmission in the substrate. The geometry with grating on top of the waveguide, shown in Figure 29(b), is preferred to the commonly observed geometry with etched grating on thicker waveguide, shown in Figure 29(a), in order to minimize wave impedance

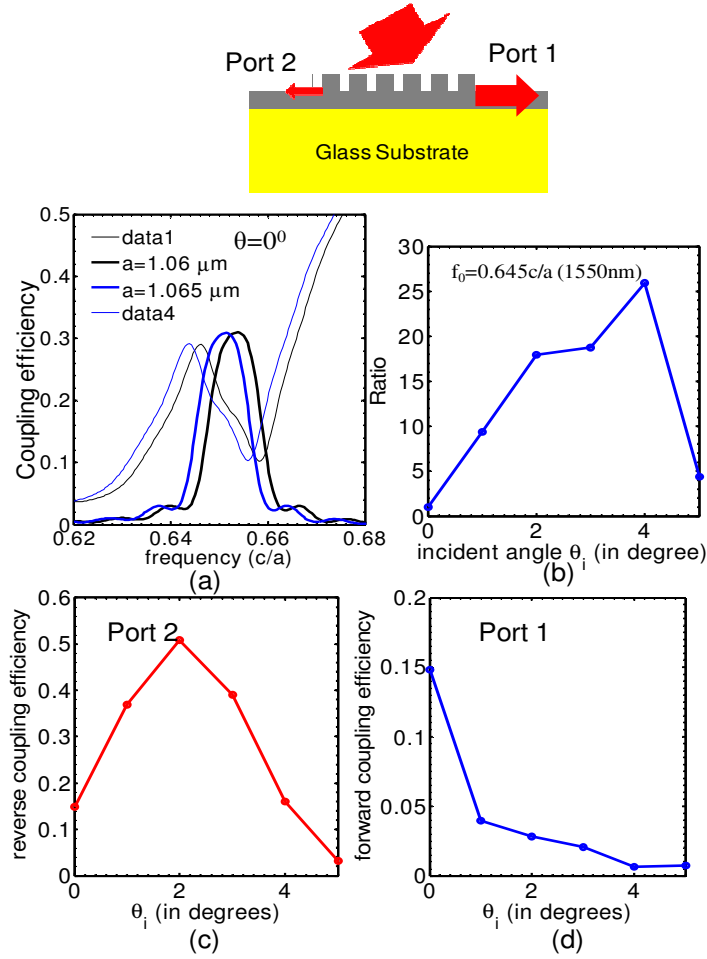


Figure 30 2D FDTD simulated Design of the grating coupler to determine angle by ratio method. Si on glass implementation (a) The spectrum of the coupled and the transmitted light for normal incidence. The period  $\Lambda$  being 1.065  $\mu\text{m}$ , Si filling fraction  $ff=0.22$  and grating thickness  $tg=0.26\mu\text{m}$ , waveguide thickness  $twg=0.22\mu\text{m}$ , the number of grating periods  $N=31$ , the size of the gaussian source beam  $26\Lambda$  with Gaussian beam diameter  $=26*0.9*\Lambda$  and index of the oxide substrate  $nox=1.48$ . (b) The ratio between the Port 2 and Port 1 coupled power. Variation of coupling efficiency with incident angle in (c) Port 2 and (d) Port 1

mismatch between the grating section  $Z_g$  and the waveguide section  $Z_{wg}$ . Figure 29(c) is the broadband reflection spectrum of the grating used for the coupler. The period  $\Lambda$  being 1.05  $\mu\text{m}$ , Si filling fraction  $ff=0.2$ , grating thickness  $tg=0.26\mu\text{m}$  and the index of silicon  $n_{Si}=3.48$ . Figure 29(d) shows the effect of waveguide thickness  $twg$  on the grating coupler performance. The period  $\Lambda$  being 1.04  $\mu\text{m}$ , Si filling fraction  $ff=0.17$  and grating thickness  $tg=0.26\mu\text{m}$ , the number of grating periods  $N=31$ , the size of the Gaussian source beam  $26\Lambda$  with Gaussian beam



diameter= $26 \times 0.9 \times \Lambda$  and index of the oxide substrate  $n_{ox}=1.48$ . The source is being kept at a distance  $0.25 \mu\text{m}$  above the grating. The Transmission  $T$  within the glass substrate increases with the waveguide thickness  $t_{wg}$ , so in our designs the  $t_{wg}$  is kept constant, equal to  $0.22 \mu\text{m}$ , where transmission  $T$  is relatively lower and this thickness is widely used for single mode operation in Silicon photonics. Unless specified, henceforth, for tuning the frequency of the coupled light the period of the grating  $\Lambda$  is varied.

#### *4.3.1 Angle Detection for predetermined Laser power: Si on Glass Implementation*

A design implementation with Silicon on glass substrate is shown in Figure 30. The period  $\Lambda$  being  $1.065 \mu\text{m}$ , Si filling fraction  $ff=0.22$  and grating thickness  $t_g=0.26 \mu\text{m}$ , waveguide thickness  $t_{wg}=0.22 \mu\text{m}$ , the number of grating periods  $N=31$ , the size of the gaussian source beam  $26\Lambda$  with Gaussian beam diameter= $26 \times 0.9 \times \Lambda$  and index of the oxide substrate  $n_{ox}=1.48$ . The source is being kept at a distance  $0.25 \mu\text{m}$  above the grating. Henceforth unless specified, the source specification remains the same. Figure 30(b) shows the increase of power ratio with incident angle till 4 degree. From Figure 30 (c) and (d) it's evident that the coupler is negatively detuned. In Figure 30(b) there is a sharp decrease of the ratio from incident angle 4 to 5 degree due to increased separations between the Port1 and Port 2 coupling resonances. So this device can work well for a laser source with pre-calibrated and predetermined power. As soon as the minimum power coupled within the grating falls below a threshold the angle cannot be determined. However for an arbitrary laser beam a support grating is required which will determine that whether this decline in ratio is for higher or lower angles. This will be discussed in proceeding section.

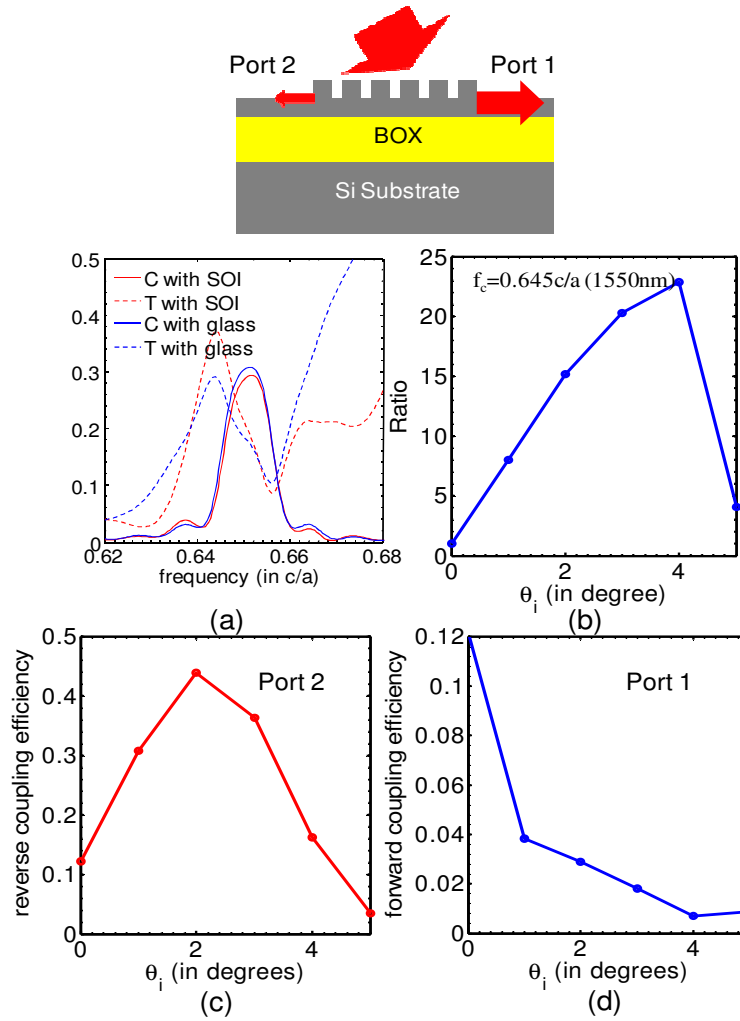


Figure 31 2D FDTD simulated Design of the grating coupler on SOI to determine angle by ratio method. (a) The spectrum of the coupled and the transmitted light for normal incidence. (b) The ratio between the Port 2 and Port 1 coupled power. Variation of coupling efficiency with incident angle in (c) Port 2 and (d) Port 1

#### 4.3.2 Angle Detection for predetermined Laser power: SOI Implementation

Figure 31 summarizes the angle detection performance with grating designed on SOI. Since a Broadband reflector is used as a grating the transmitted light should be less hence the interference from the Silicon substrate should not be much of an issue. This is shown in Figure 31(a) that with SOI there is slight increase of the transmitted power in the window of interest. The Transmission in the case of SOI is obtained by subtracting the coupled power and the reflected

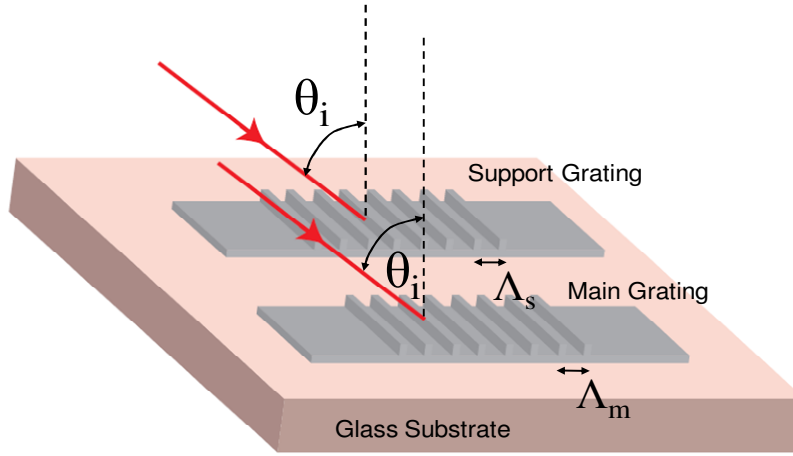


Figure 32 Schematic to illustrate the detection of angle of incidence  $\theta_i$  of any arbitrary Laser. The main grating is used calculate the ratio of coupled in the two waveguide ports. The support grating determines that whether the incidence angle is on the higher or in the lower side. The two gratings differs in the period only. For our design  $\Lambda_s=1.05\mu\text{m}$  and  $\Lambda_m=1.065\mu\text{m}$ .

power from 1. As discussed before, due to the dip in ratio from 4 degree to 5 degree this can be used only within various instrumentations where the incident laser beam is precalibrated.

#### 4.3.3 Angle Detection for arbitrary Laser power

The principle is illustrated in Figure 32 where two grating couplers, main and support are used to determine that whether the incidence angle is on the higher or lower side. The results of the angle detection by main grating fortified by support grating are illustrated in Figure 33. In summary when the support grating receives more power than the main grating the angle of incidence lies on the higher side between 3 and 4.5 degree. Beyond this angle, the coupling efficiency of the main grating is very low and should be avoided if the ratio between the powers in Port2 and Port 1 is not very high, like greater than 12. The same implementation in SOI is shown in Figure 34. Though the period and the Gaussian source sizes in the simulations are different, they differ only slightly because the periods of the gratings are very close to each other ( $\Lambda_s=1.05\mu\text{m}$  and  $\Lambda_m=1.065\mu\text{m}$ ). In both the cases the Gaussian source size is maintained as 26 times  $\Lambda_i$ , where  $\Lambda_i=\Lambda_s=1.05\mu\text{m}$  for the support grating and  $\Lambda_i=\Lambda_m=1.065\mu\text{m}$  for the main grating. The incident powers from the two sources are 6.16 a.u. and 6.257 a.u. respectively, which are sufficiently close to say that performance will not be very different had they been kept equal. This

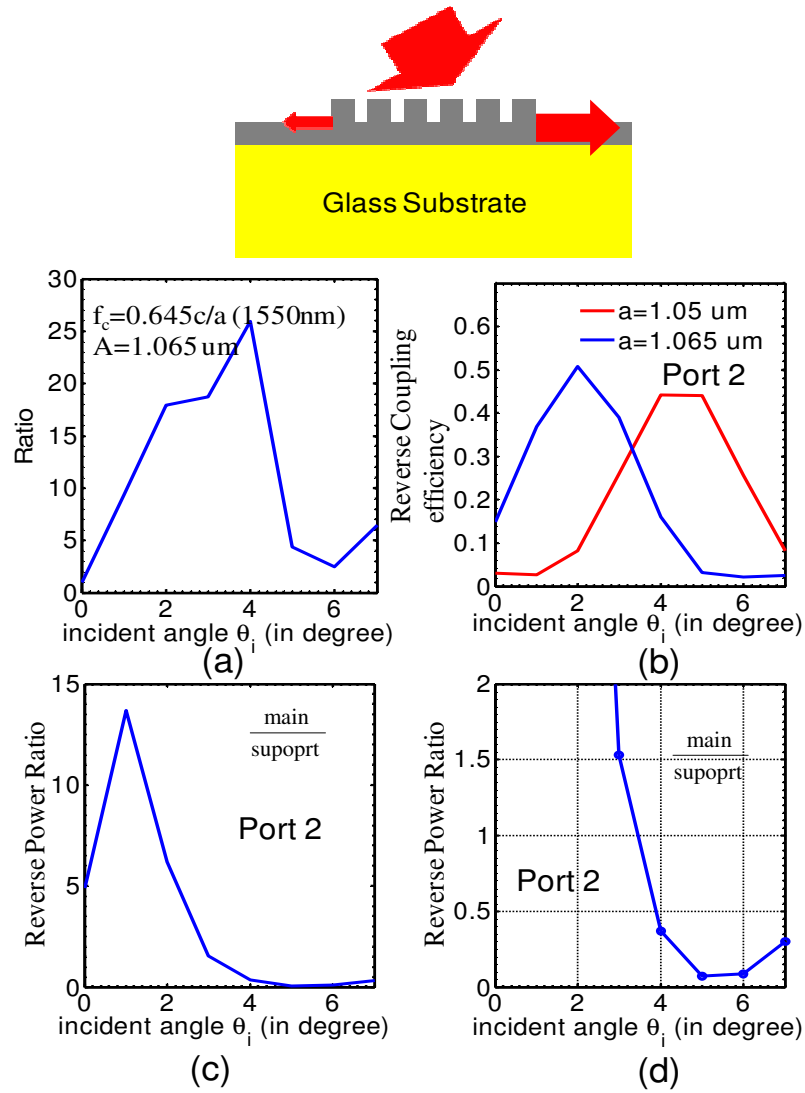


Figure 33 2D FDTD simulated Results of the grating coupler on glass substrate to determine angle by ratio method of any arbitrary Laser. (a) The ratio between the Port 2 and Port 1 coupled power of the main grating. The main grating period  $\Lambda_m$  being  $1.065 \mu m$ , the support grating period  $\Lambda_s = 1.050 \mu m$ , Si filling fraction  $ff = 0.22$  and grating thickness  $t_g = 0.26 \mu m$ , waveguide thickness  $t_{wg} = 0.22 \mu m$ , the number of grating periods  $N = 31$ , (b) Variation of coupling efficiency with incident angle in Port 2 for the support and main grating (c) The ratio between the Port 2 coupled powers of the main and support grating (d) The magnified version of the (c) indicating that when the support grating receives more power the incident angle is greater than 3 degree.

issue depends on the scenario that whether the apertures of the main and the support gratings are kept equal or different, but in either of the cases the results only differ slightly.

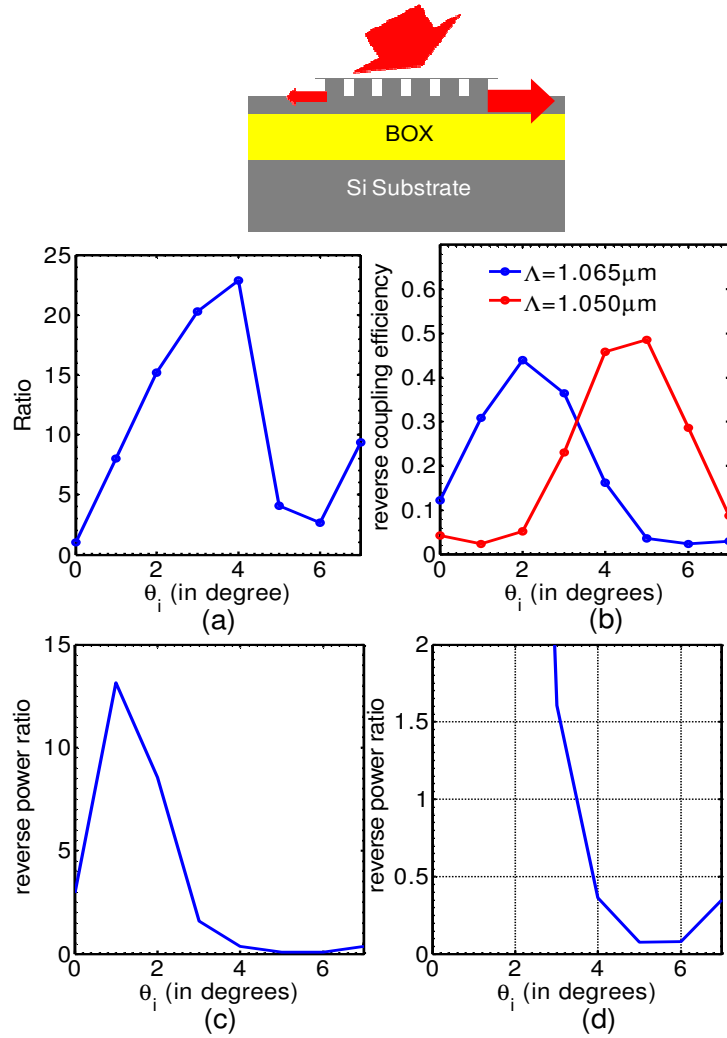


Figure 34 2D FDTD simulated Results of the grating coupler on SOI to determine angle by ratio method of any arbitrary Laser. (a) The ratio between the Port 2 and Port 1 coupled power of the main grating. The main grating period  $\Lambda_m$  being  $1.065 \mu\text{m}$ , the support grating period  $\Lambda_s = 1.050 \mu\text{m}$ , Si filling fraction  $ff = 0.22$  and grating thickness  $t_g = 0.26 \mu\text{m}$ , waveguide thickness  $t_{wg} = 0.22 \mu\text{m}$ , the number of grating periods  $N = 31$ , (b) Variation of coupling efficiency with incident angle in Port 2 for the support and main grating (c) The ratio between the Port 2 coupled powers of the main and support grating (d) The magnified version of the (c) indicating that when the support grating receives more power the incident angle is greater than 3 degree.

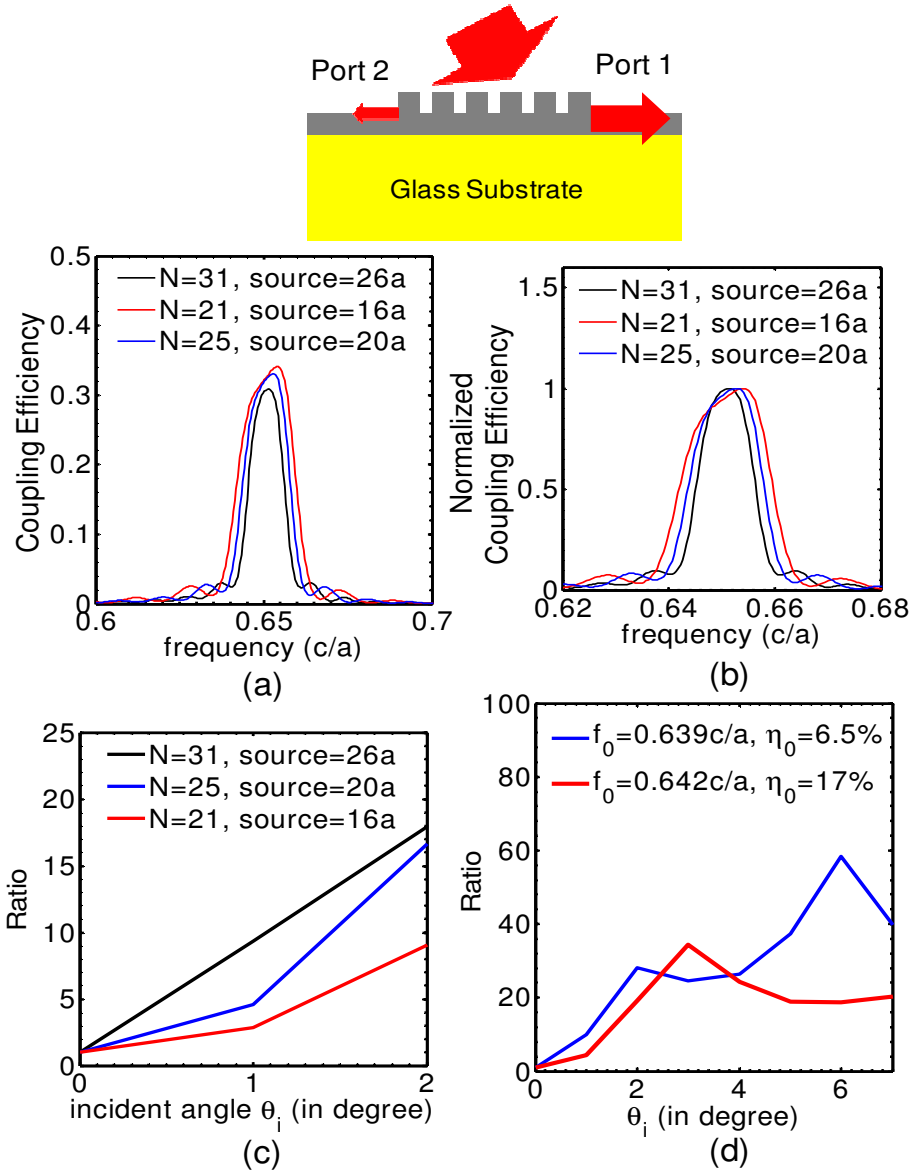


Figure 35 2D FDTD simulated Results of the grating coupler analyzing its sensitivity to detect the angles (a) The single side coupling efficiency at surface normal incidence  $\theta_i=0^\circ$  for different number of grating periods  $N$  and source width. The grating period  $\Lambda$  being  $1.065 \mu\text{m}$ , Si filling fraction  $ff=0.2$  and grating thickness  $t_g=0.26\mu\text{m}$ , waveguide thickness  $t_{wg}=0.22 \mu\text{m}$ , (b) The normalized coupling efficiency for different number of grating periods  $N$  and source width indicating that the linewidth decreases with increase in number of gratings  $N$  (c) The ratio between the Port 2 and Port 1 coupled power for different number of grating periods  $N$  and source width indicating that the angular sensitivity increases with increase in  $N$ . The frequency being  $f_0=0.645(c/a)$  (d) The ratio between the Port 2 and Port 1 coupled power for  $N=21$  and source width  $=16\Lambda$ , for two different frequencies.  $\eta_0$  being the single side coupling efficiency for surface normal incidence  $\theta_i=0^\circ$

#### 4.4 Sensitivity analysis of the grating coupler based angle detector

Figure 35 presents the sensitivity analysis of the second order grating coupler as an angle detector. The period  $\Lambda$  being  $1.065 \mu\text{m}$ , Si filling fraction  $ff=0.22$  and grating thickness  $t_g=0.26\mu\text{m}$ , waveguide thickness  $t_{wg}=0.22 \mu\text{m}$ , Gaussian beam radius of the source is kept at 0.9 times source width and index of the oxide substrate  $n_{ox}=1.48$ . The source is being kept at a distance  $0.25 \mu\text{m}$  above the grating. From Figure 35 (a) and (b), it is observed that with increase in number of the grating periods  $N$  and the source size the coupling efficiency and the linewidth reduces, due to the filtering effect. So as the linewidth decreases with coupler size the sensitivity to the small angle change also increases for the grating coupler. This is reflected in the plot of Figure 35(c). The slope of the ratio of the coupled power, between the two ports, increases with the device size. The frequency of the incident beam is  $0.645 (c/a)$ .

Figure 35(d) shows that the range of angle that can be covered by monotonically increasing ratio between the two coupled ports depends on the point of observation within the coupled resonance. Here the number of the grating period  $N=21$  and the source width is 16 periods. So at a frequency  $f_0=0.642(c/a)$ , the surface normal coupling efficiency  $\eta_0$  being 17% the ratio starts decreasing after  $3^\circ$  angle of incidence. On the other hand if the starting point was at  $f_0=0.639 (c/a)$ , where the  $\eta_0$  is 6.5%, it gets more scope to obtain an increasing ratio with higher range of angles. This is reflected in Figure 35(d), where the ratio of the coupled power increases till  $6^\circ$ , for the frequency  $f_0=0.639 (c/a)$ . However there is a sudden jump of the ratio at  $2^\circ$ , which may be due to the lack of smoothness of the coupled resonance line shape and this glitch can be successfully by passed by the use of a support grating coupler.

#### 4.5 Conclusion

A comprehensive design aspect has been presented in this chapter to use a second order grating coupler as a laser beam angle detector. Such a coupler can achieve fast responding on-chip detection of the laser beam steering. The range of the angle that can be determined by this

method depends on the linewidth of the coupled resonance, the laser power and the detector sensitivity.



## CHAPTER 5

### DESIGN OF A 2D GRATING COUPLER FOR POLARIZATION DETECTION

#### 5.1 Introduction

Infrared detectors are extremely important components for thermal imaging system. Conventional infrared detectors are successful in resolving low contrast images of the terrestrial scenes. A detector which provides the intensity and the polarization data of the infrared radiation is extremely useful in the fields of high contrast infrared imaging and zero  $\Delta T$  imaging. Such a detector can suppress the unpolarized background radiation and finds immense applications in the fields of mine field detection, oceanography, material characterizations and robot vision.

Conventionally, a rotating polarizer is used in front of the photodetector to determine the polarization of the radiation, this process is not only clumsy but also not fast enough to give information regarding a fast moving objects. One common way to determine the polarization of the incident radiation is to fabricate gratings in front of the active region of the photodetectors [58]. But such detectors fail to work in an illuminated or semi illuminated atmosphere. Other approaches like focusing grating couplers [59], 2D first order grating couplers [24] polarization splitting based grating coupler [60] though all reveals the state of polarization of the incident radiation they don't reveals any information regarding the direction of the incident beam and they are all optimized to couple the obliquely incident light. However, for the imaging purposes it is preferred if the camera can able to discern that what lies in front of it. For the case of focused grating [59], two gratings are used which decreases the resolution of the camera all the more, and the coupling efficiency of the TE/TM are generally different which requires further scaling to get accurate state of polarization. Moreover, Laser polarization spectroscopy [61-62], is used to detect the anisotropies within the materials and gas molecules. In recent years active-imaging has made a very strong impact in the fields of night vision and underwater imaging due

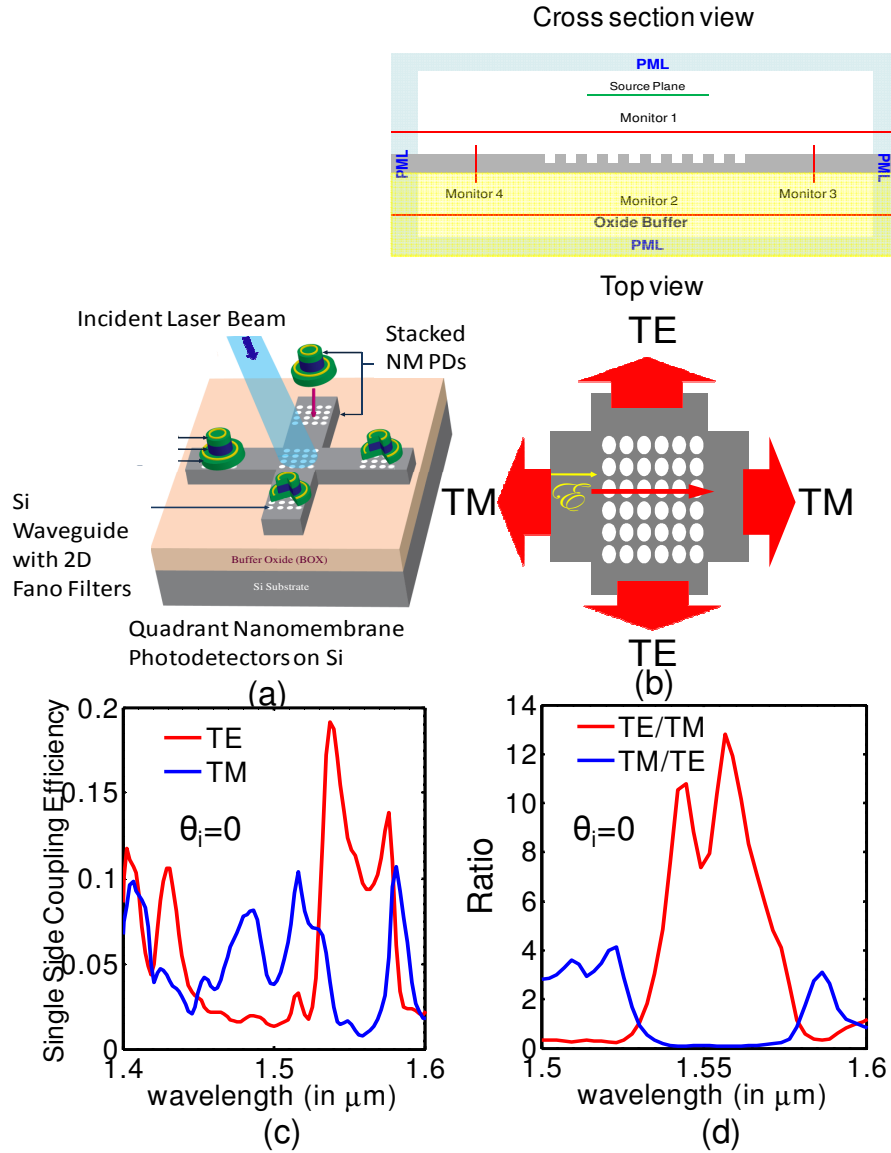


Figure 36 (a) The schematic of the 2D second order grating coupler to detect the polarization (b) (top) The cross-section of the 3D FDTD computational cell. Note that in the computation silicon on glass substrate is considered (Down) The top view of the 2D grating depicting the definition of polarization (c) The 3D FDTD simulated coupling efficiency within each waveguide, for surface normal incidence. The grating period  $\Lambda=0.955 \mu$ , radius  $r=0.26\Lambda$ , top grating thickness  $t_g=0.34\mu\text{m}$ , the waveguide thickness  $t_{wg}=0.34\mu\text{m}$ , silicon refractive index  $n_{\text{Si}}=3.48$  and glass/oxide refractive index  $n_{\text{ox}}=1.48$ , the number of grating periods  $N=25$ , the size of the gaussian source beam  $24\Lambda$  with Gaussian beam radius  $=24*0.9*\Lambda$  (d) The ratio between of the coupled power with orthogonal polarizations

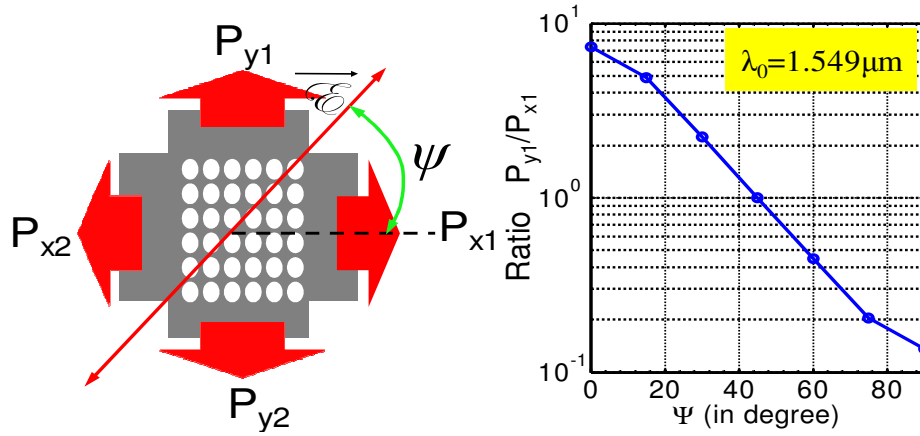


Figure 37 The variation of the ratio of the coupled power within the two adjacent waveguides for different values of polarization angles  $\psi$ . The wavelength is  $1.549\mu\text{m}$

to its ability to see through the glass. The polarization information in the field of active imaging has found tremendous applications to produce high contrast images to detect the concealed objects inside the vegetations or bushes. In this paper, we have designed a 2D second order grating coupler to couple normally incident light with a high contrast in TE over TM polarization. With the coupler based detector, the direction of a bright source can be accurately determined without much complexity.

## 5.2 2D Grating coupler design to detect the incident polarization

### 5.2.1 Silicon on Glass Implementation

Figure 36(a) shows the schematic of the 2D second order grating coupler to detect the polarization of the incident beam. Figure 36(b) shows the cross-sectional view of the FDTD computational cell where we have used silicon on glass substrate as the device model. The coupling efficiency within each of waveguide for two different polarizations is shown in Figure 36(c). The grating period  $\Lambda=0.955\ \mu$ , radius  $r=0.26\Lambda$ , top grating thickness  $t_g=0.34\mu\text{m}$ , the waveguide thickness  $t_{wg}=0.34\mu\text{m}$ , silicon refractive index  $n_{Si}=3.48$  and glass/oxide refractive index  $n_{ox}=1.48$ , the number of grating periods  $N=25$ , the size of the gaussian source beam  $24\Lambda$  with Gaussian beam radius  $=24*0.9*\Lambda$ . The peak coupling efficiency of 19.2% for TE polarization is observed at the wavelength  $1.537\mu\text{m}$ . A high contrast ratio of 7.4 to 12.8, between the two orthogonal polarizations is observed within the wavelength range  $1.54\mu\text{m}$  to  $1.565\ \mu\text{m}$ . This is

reported in Figure 36(d). Figure 37 shows variation of the ratio of the coupled power within the two adjacent waveguides for different values of polarization angles  $\psi$ . The design wavelength is  $1.549\mu\text{m}$ . At this wavelength the ratio between the coupled powers of two polarizations is 7.4.

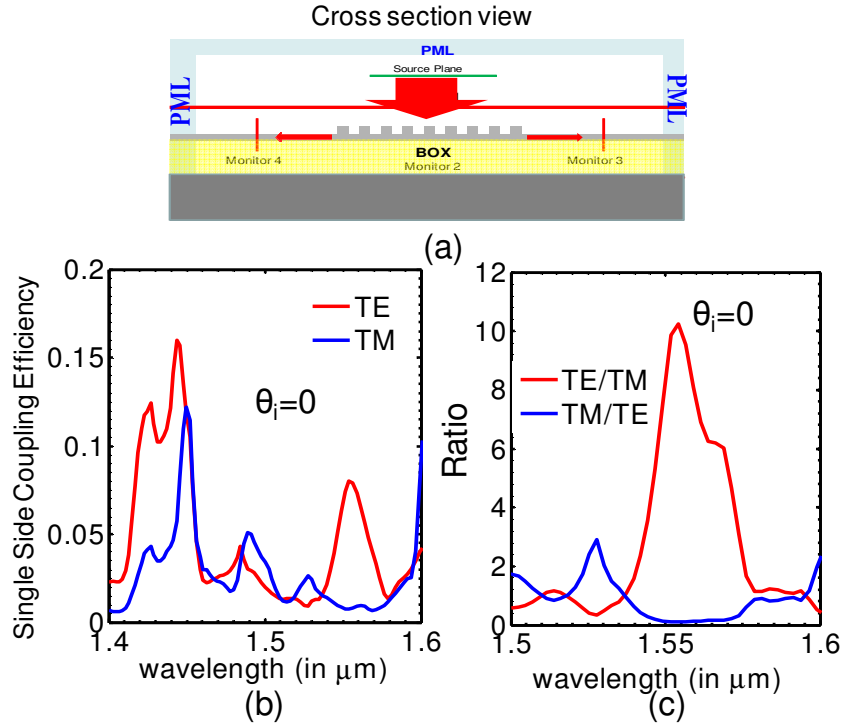


Figure 38 (a) The schematic cross-section of the 3D FDTD computational cell. Note that in the computation SOI is considered (b) 3D FDTD simulated coupling efficiency within each waveguide, for surface normal incidence. The grating period  $\Lambda=0.955\mu$ , radius  $r=0.26\Lambda$ , top grating thickness  $t_g=0.34\mu\text{m}$ , the waveguide thickness  $t_{wg}=0.34\mu\text{m}$ , the BOX layer thickness= $2.0\mu\text{m}$ , silicon refractive index  $n_{\text{Si}}=3.48$  and glass/oxide refractive index  $n_{\text{ox}}=1.48$ , the number of grating periods  $N=25$ , the size of the gaussian source beam  $24\Lambda$  with Gaussian beam radius= $24*0.9*\Lambda$  (c) The ratio between of the coupled power with orthogonal polarizations

### 5.2.2 Silicon on Insulator (SOI) Implementation

The same implementation with SOI (Silicon on Insulator) is presented in Figure 38. The thickness of the BOX layer is considered to be  $2.0\mu\text{m}$ . Figure 38(b) shows that the coupling efficiency of both polarizations have reduced due to the interference of the coupled light, with reflected light from the Si substrate. The peak coupling efficiency is 8% for TE polarization at  $1.554\mu\text{m}$ . However the contrast ratio between the coupled powers of two orthogonal polarizations

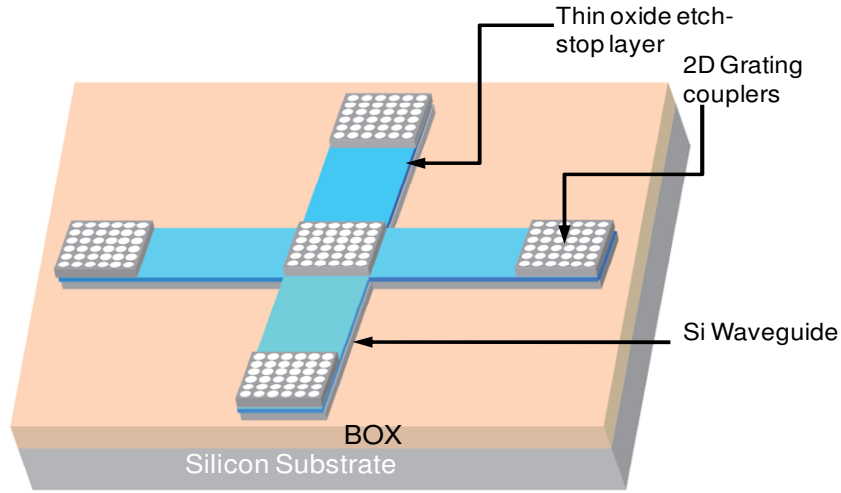


Figure 39 The schematic of the 2D second order grating coupler to detect the polarization with etch stop layer in between the 2D gratings and the waveguide.

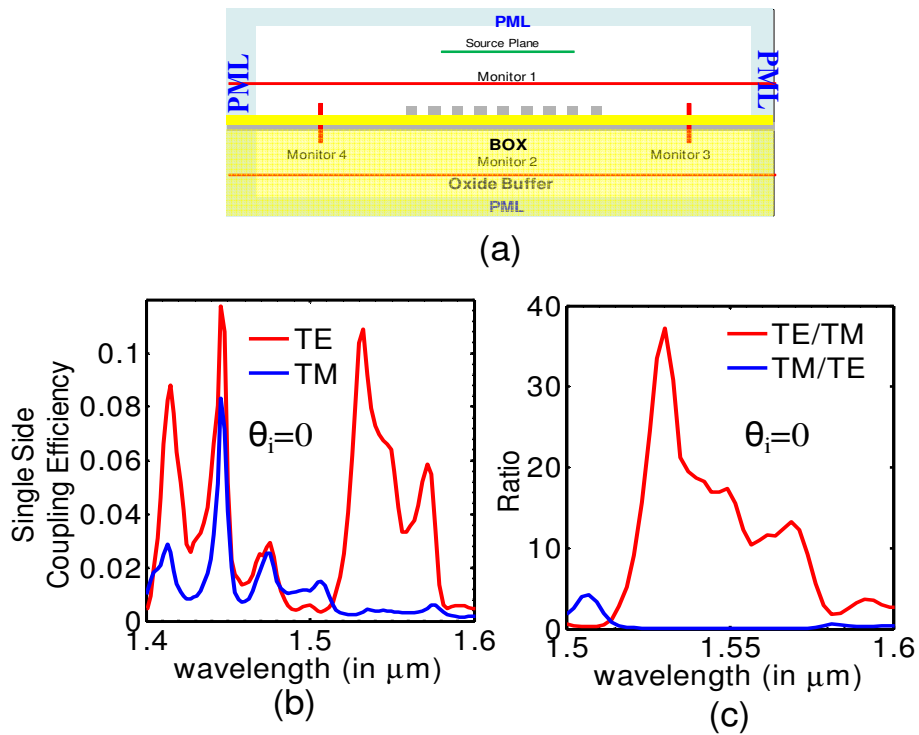


Figure 40 The schematic of the 2D second order grating coupler with thin etch stop layer, to detect the polarization (a) The cross-section of the 3D FDTD computational cell. Note that in the computation silicon on glass substrate is considered (b) The 3D FDTD simulated coupling efficiency within each waveguide, for surface normal incidence. The grating period  $\Lambda=0.955 \mu$ , radius  $r=0.26\Lambda$ , top grating thickness  $t_g=0.34\mu$ , the waveguide thickness  $t_{wg}=0.34\mu$ , the oxide etch stop layer=30 nm, silicon refractive index  $n_{Si}=3.48$  and glass/oxide refractive index  $n_{ox}=1.48$ , the number of grating periods  $N=25$ , the size of the gaussian source beam  $24\Lambda$  with Gaussian beam radius= $24*0.9*\Lambda$  (c) The ratio between of the coupled power with orthogonal polarizations

is still high. The ratio ranges from 5.5 to 10.25 within the wavelength range of 1.547 $\mu\text{m}$  to 1.569 $\mu\text{m}$ , as shown in Figure 38(c).

The above mentioned scheme for polarization detection involves the partial etching of the Silicon to form 2D photonic Crystal. In this kind of fabrications, the etching depth in many a times difficult to control and the device performance is extremely sensitive to the etch depth error. However for the purpose of uncontrolled etching and optical characterization a thin etch stop layer between the 2D grating or 2D PCS (photonic crystal slab) and the waveguide layer is preferred as shown in Figure 39.

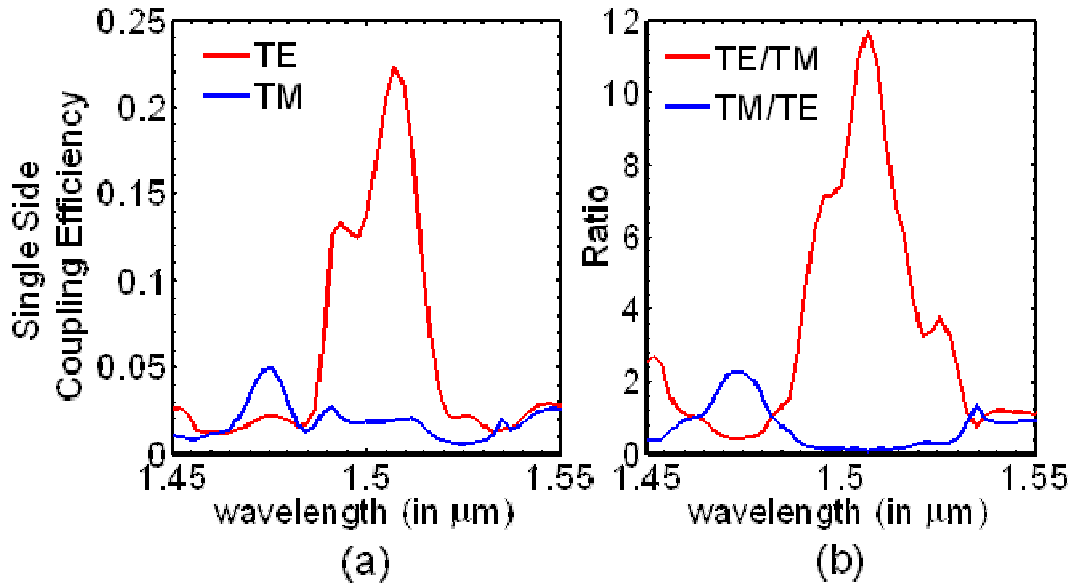


Figure 41 FDTD simulated results for 2D second order grating coupler with thin etch stop layer, with enhanced coupling efficiency. The grating period  $\Lambda=1.4 \mu$ , radius  $r=0.35\Lambda$ , top grating thickness  $t_g=0.34\mu\text{m}$ , the waveguide thickness  $t_{wg}=0.34\mu\text{m}$ , the oxide etch stop layer=30 nm, Number of grating periods is 25 (a) The 3D FDTD simulated coupling efficiency within each waveguide, for surface normal incidence (b) The ratio between of the coupled power with orthogonal polarizations

The full-wave 3D FDTD simulated result is shown in Figure 40. Its observed in Figure 40(b), that the peak coupling efficiency of the TE mode has decreased from 19.2% to 11%, however the ratio between TE-TM power coupled has increased. So in order to increase the coupling efficiency we have simulated new parameters the results are shown in Figure 41.

The grating period  $\Lambda=1.4 \mu\text{m}$ , radius  $r=0.35\Lambda$ , top grating thickness  $t_g=0.34\mu\text{m}$ , the waveguide thickness  $t_{wg}=0.34\mu\text{m}$ , silicon refractive index  $n_{\text{Si}}=3.48$  and glass/oxide refractive index  $n_{\text{ox}}=1.48$ , the number of grating periods  $N=25$ , the size of the gaussian source beam  $24\Lambda$  with Gaussian beam radius= $24*0.9*\Lambda$  The peak coupling efficiency of 24% for TE polarization is observed at the wavelength  $1.51\mu\text{m}$ . A high contrast ratio of 7.2 to 11 between the two orthogonal polarizations is observed within the wavelength range of 25nm, the center wavelength being  $1.5\mu\text{m}$ . In order to get the peak coupling efficiency at  $1.55 \mu\text{m}$ , the period has to be increased,

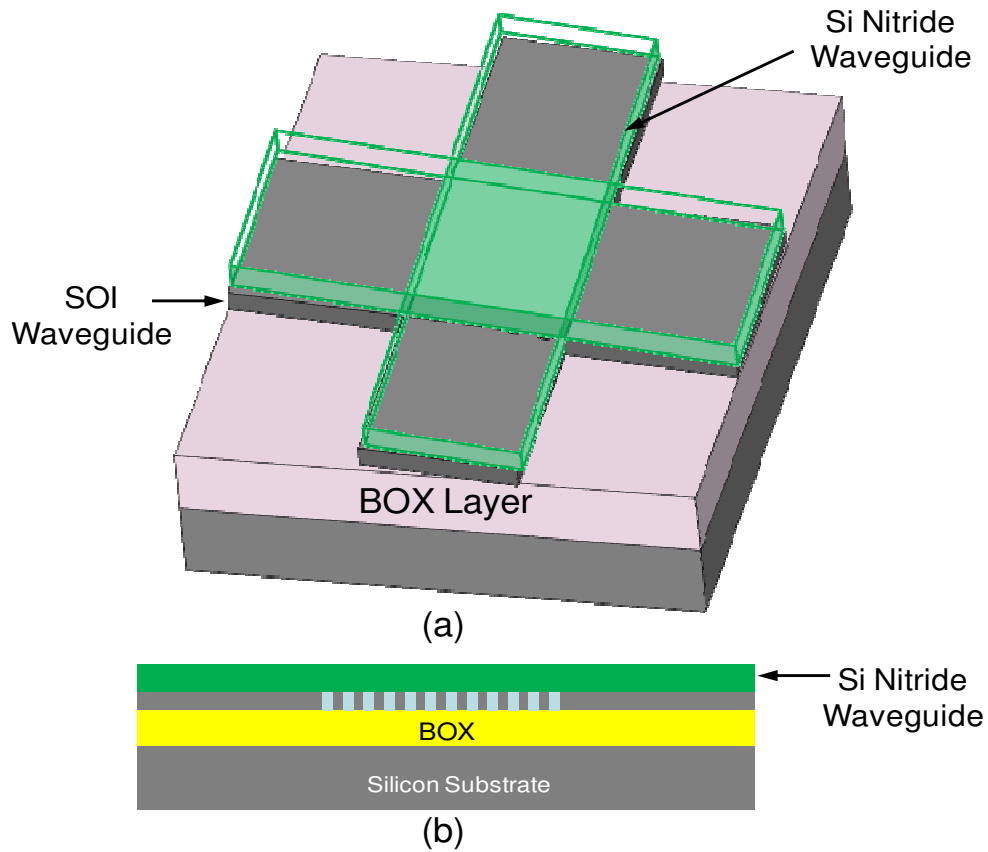


Figure 42 (a) The schematic of the 2D second order nitide on SOI grating coupler (b) The cross-section of the device.

which makes the structure very large, even for a large parallel computation cluster to solve the problem. However reducing the number of periods from 25 to 17 shows that a period of  $\Lambda=1.445 \mu\text{m}$ , provides a peak coupling efficiency at wavelength  $1.55 \mu\text{m}$ . So considering  $\Lambda=1.445 \mu\text{m}$ , on SOI substrate with BOX layer thickness of  $2.0\mu\text{m}$ , simulating the 3D structure with

continuous source reveals a TE mode coupling efficiency of 12.5% and a polarization contrast ratio being 11.

### 5.2.3 Nitride on Silicon on Insulator (SOI) Implementation

In this section we will present the design of a 2D vertical grating coupler with nitride on SOI architecture. The device is of particular interest due to its capability to couple light from the free space to the nanophotonic waveguide and for on-chip beam routing. The device schematic and its cross-section is shown in Figure 42.

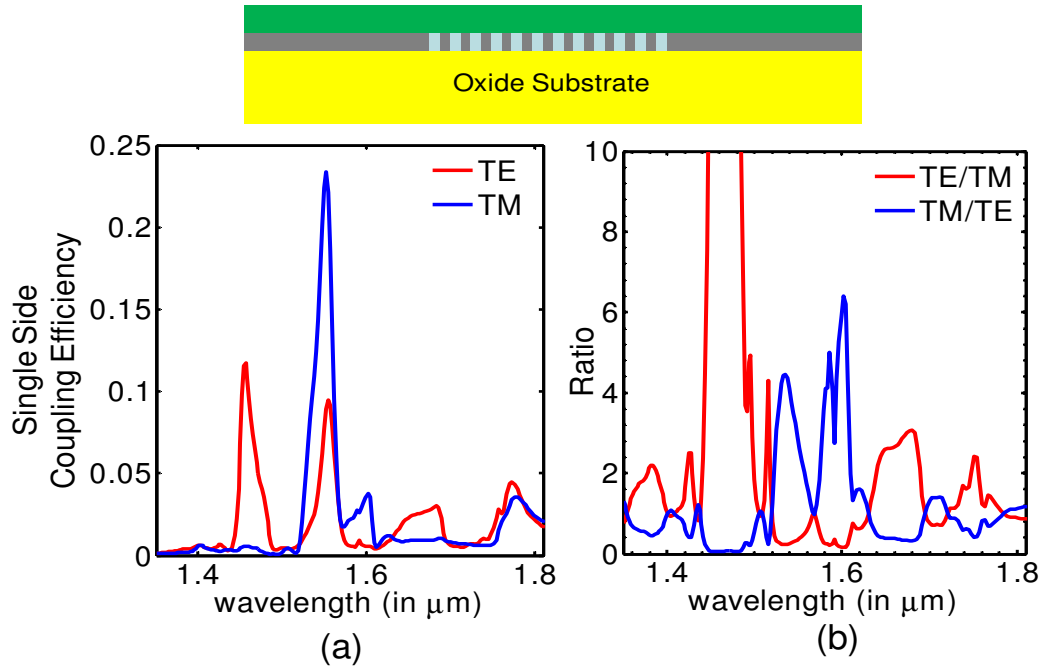


Figure 43 FDTD simulated results for 2D second order grating coupler with nitride on Silicon configuration. The substrate is chosen to be glass. The grating period  $\Lambda=0.98 \mu\text{m}$ , radius  $r=0.25\Lambda$ , Si grating thickness  $t_g=0.34\mu\text{m}$ , the nitride waveguide thickness  $t_{wg}=0.35\mu\text{m}$ , Number of grating periods is 25 (a) The 3D FDTD simulated coupling efficiency within each waveguide, for surface normal incidence (b) The ratio between of the coupled power with orthogonal polarizations

The device is extremely easy to fabricate and suitable for high-yield production. The 2D photonic crystal is first etched within the Silicon and then some silica particles are filled within the holes of the photonic Crystal and then the Silicon nitride waveguide can be made by nitride deposition and transferring pattern by photolithography.



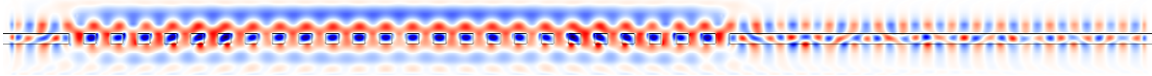


Figure 44 The field plot of the coupled light within the 2D grating coupler with nitride on Si configuration

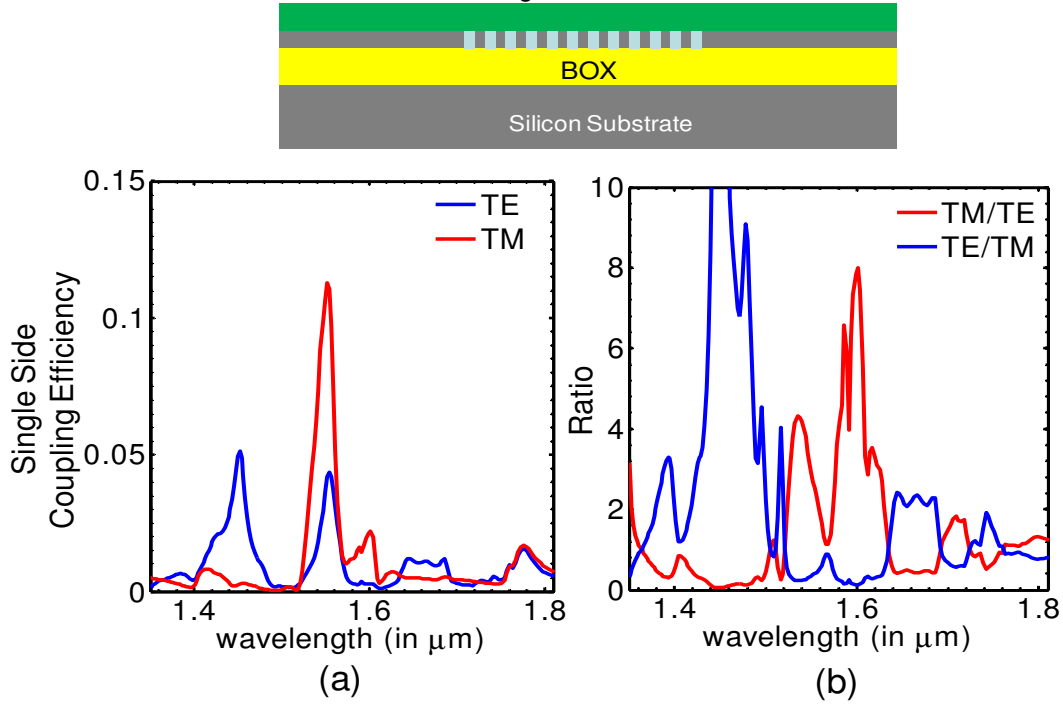


Figure 45 FDTD simulated results for 2D second order grating coupler with nitride on SOI configuration. The grating period  $\Lambda=0.98 \mu\text{m}$ , radius  $r=0.25\Lambda$ , Si grating thickness  $t_g=0.34\mu\text{m}$ , the nitride waveguide thickness  $t_{wg}=0.35\mu\text{m}$ , The BOX thickness= $2.0\mu\text{m}$ , Number of grating periods is 25 (a) The 3D FDTD simulated coupling efficiency within each waveguide, for surface normal incidence (b) The ratio between of the coupled power with orthogonal polarizations

The FDTD simulated coupling efficiency for nitride on Silicon grating configuration, considering glass substrate is shown in Figure 43. The grating period  $\Lambda=0.98 \mu\text{m}$ , radius  $r=0.25\Lambda$ , Silicon grating thickness  $t_g=0.34\mu\text{m}$ , the top nitride waveguide thickness  $t_{wg}=0.34\mu\text{m}$ , silicon refractive index  $n_{\text{Si}}=3.48$  and glass/oxide refractive index  $n_{\text{ox}}=1.48$ , the index within the holes due to silica particles=1.2, the index of the nitride=1.96, the number of grating periods  $N=25$ , the size of the gaussian source beam  $24\Lambda$  with Gaussian beam radius= $24*0.9*\Lambda$  The peak coupling efficiency of 24% for TE polarization is observed at the wavelength  $1.55\mu\text{m}$ . However the polarization contrast is poor in the wavelength of interest as shown in Figure 43(b).

The field plot of the coupled light at  $1.55\mu\text{m}$  within Nitride-on-Si 2D grating coupler is shown in Figure 44.

When the above structure is simulated considering SOI as the substrate, with BOX layer thickness of  $2\mu\text{m}$ , the result is shown in Figure 45. The peak coupling efficiency has reduced to 12% at  $1.55\mu\text{m}$ , due the interference from the light reflected from the BOX-Si Substrate interface.

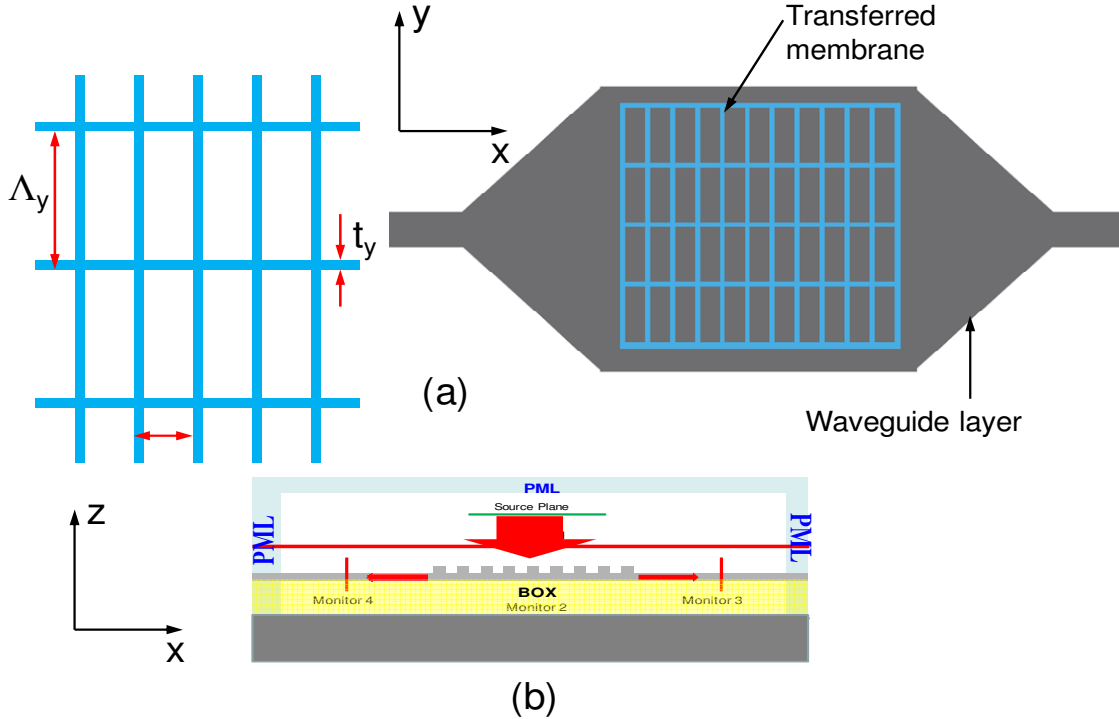


Figure 46 The schematic of the Quasi 2D second order grating coupler (a) (left) the parameters of the transferred membrane (right) the top view of the coupler (b) The cross-section of the device.

#### 5.2.4 Quasi 2D grating coupler based on transferred nanomembrane

Sometimes high coupling efficiency is required for coupling even at the cost of polarization independence. Generally, 1D grating couplers, though polarization dependent, provides high coupling efficiency. However to avoid partial controlled etching of Silicon, the transferred nanomembrane is preferred as discussed in the previous chapters. However during the release of the nanomembrane from the buried oxide, when treated with the BHF, the gratings starts moving which destroys the whole periodicity of the structure. Hence, connected structures, like 2D photonic crystals are more preferable for the release and the transfer process.

Hence the Quasi-2D grating coupler is designed as shown in Figure 46, such a grating can be transferred easily, because of its connected lattice.

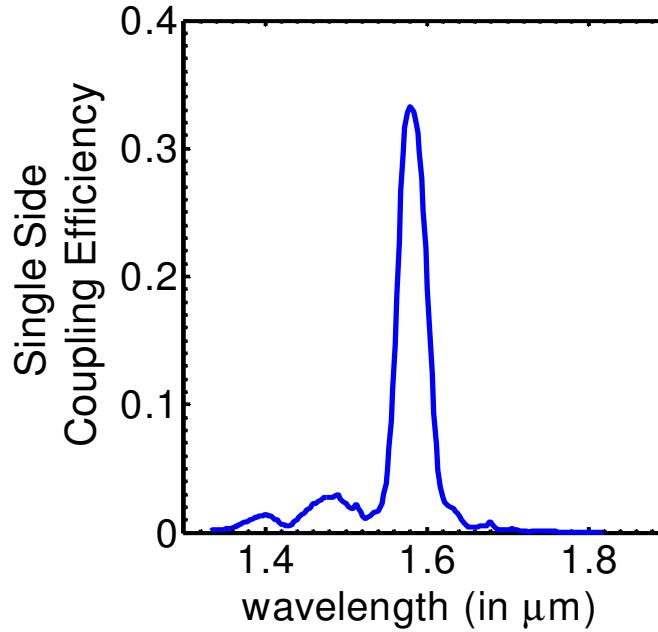


Figure 47 The 3D FDTD simulated coupling efficiency within each waveguide, the mode being TE-like, i.e. excitation has  $\mathbf{E}_y$  component

Figure 47 shows the FDTD computed coupling efficiency for  $\mathbf{E}_y$  excitation, the single side coupling efficiency being 33% at the wavelength of 1580nm. The grating period  $\Lambda_x=1.065 \mu\text{m}$ , radius  $\Lambda_y=3.5 \mu\text{m}$ , Silicon grating thickness  $t_g=0.26\mu\text{m}$ , the bottom Silicon waveguide thickness  $t_{wg}=0.26\mu\text{m}$ ,  $t_y=150 \text{ nm}$ , silicon refractive index  $n_{\text{Si}}=3.48$  and glass/oxide refractive index  $n_{\text{ox}}=1.48$ , the number of grating periods  $N_x=21$ ,  $N_y=7$  in the x and y direction respectively, the size of the gaussian source beam  $20\Lambda$  with Gaussian beam radius= $24*0.45*\Lambda$ . With a proper combiner like a racetrack resonator the power from the two ports can be added to get an enhanced unidirectional efficiency of 66%.

### 5.3 Conclusion

In summary we have designed several variations of 2D second order grating couplers which can couple surface normal incident light with high coupling efficiency contrast between the two orthogonal polarizations. The device can work in illuminated or semi-illuminated environment.

It gives information regarding the direction of the incident source. The direction of the incident radiation from a bright source can be easily detected by the 2D grating coupler based detector.

## CHAPTER 6

### CONCLUSION AND PERSPECTIVES

In this final chapter we summarize the major results of our research and also, present the future perspectives which can be realized from the results that we have obtained so far.

#### 6.1 Conclusion

The main purpose of this research is the design of multi-directional light couplers for high speed optical interconnects by means of nanomembrane photonic integration. In Chapter 2 we presented the design of a high efficiency grating coupler based on transferred Silicon nanomembrane to avoid the complications of controlled partial etching within the Silicon photonic waveguides. Various issues of enhancing the efficiency of the device has been presented, like having air buffer instead of oxide buffer, use of side DBRs and bottom reflectors. In Chapter 3, we have presented the design High Q high efficiency compact grating couplers, by means of transverse resonance and evanescent coupling. Both bidirectional and unidirectional coupling is being presented. Indeed, enhance coupling efficiency is observed due to the presence of cavity, by means of critical coupling. In Chapter 4, we have presented the design of a second order vertical coupler and its application in finding the direction of the laser beam. The range of detection of the angle of incidence can be controlled by means of proper design of the resonance frequency and the Quality factor Q. In Chapter 5, various variations of 2D grating couplers, with direction and polarization detecting capability, are designed and fabrication issues are discussed. Experiments based on deposited Silicon or transferred Si, Quasi 2D grating design for its feasibility of membrane transfer and enhanced coupling efficiency is also presented. Possibility of combining the coupled light through different branches and hence get enhanced light through a single waveguide is also discussed.

## 6.2 Perspectives

From the results presented here, several topics may be the subject of the future work. The most obvious objective, should be the experimental realization of the vertical coupler, angle and polarization detection.

A second order grating coupler for coupling light vertically distributes the light in the two branches of the waveguide equally, due to the symmetry of the structure. One investigation may be the addition of a reflector in one side of the waveguide to make it unidirectional with enhanced efficiency. Another direction of research may be the design of a compact interference based combiner to get the light from the two branches to a single waveguide. With respect to design, the efficiency may get increased with non-uniform or aperiodic structures, which is another prospect for future research.

The air gap in the case of High Q grating coupler plays a very important role. However the experimental realization of such a structure is challenging, so more practical structures designs needed to be sought after.

For angle and polarization detectors the practical realization by means of deposited Silicon or nanomembrane transfer is a subject of investigation. The transfer of grating after releasing the membrane in BHF solution is challenging since the grating starts moving in the solution. Hence Quasi 2D structures with connected lattice is more favorable.

APPENDIX A  
LIST OF PUBLICATIONS

## PUBLICATIONS

1. **Tapas K. Saha**, and W. D. Zhou, "High efficiency diffractive grating coupler based on transferred silicon nanomembrane overlay on photonic waveguide", J. Phys. D. vol 42, 085115 (2009).
2. **Tapas K. Saha**, M. Lu, Z. Ma, and W. Zhou, "Design of an Angle Detector for Laser Beams based on Grating Coupling (Invited)", Micromachines (special issue on Nanophotonics), vol. 3, 36-44 (2012).
3. **Tapas K. Saha**, M. Lu, H. Zhai, D. Zhao, W. D. Zhou and Z. Ma, "Design of a compact grating coupler with controllable linewidths via transverse resonance and evanescent field coupling", IEEE Winter 2011 Topicals on Photonic Materials and Integration Architecture, Jan. 10-12, 2011, Keystone, CO.
4. **Tapas K. Saha**, M. Lu, D. Zhao, W.D. Zhou, and Z. Ma, "Design of second order grating couplers to detect the angle and polarization of the laser beam", Photonics West 2012, San Jose, CA, Jan. 2012.
5. Arvinder Chadha, Weiquan Yang, **Tapas K. Saha**, Santhad Chuwongin, Yichen Shuai, Zhenqiang Ma, Gail J. Brown and Weidong Zhou, "Spectral selective absorption enhancement from stacked ultra-thin InGaAs/Si Fano resonance membranes ", Photonics West 2012, San Jose, CA, Jan. 2012.



## REFERENCES

- [1] W. D. Zhou, Z. Q. Ma, H. J. Yang, Z. X. Qiang, G. X. Qin, H. Q. Pang, L. Chen, W. Q. Yang, S. Chuwongin, and D. Y. Zhao, "Flexible photonic-crystal Fano filters based on transferred semiconductor nanomembranes," *Journal of Physics D-Applied Physics*, vol. 42, 2009.
- [2] H.-C. Yuan, Z. Ma, M. M. Roberts, D. E. Savage, and M. G. Lagally, "High-speed strained-single-crystal-silicon thin-film transistors on flexible polymers," *Journal of Applied Physics*, vol. 100, pp. 013708-5, 2006.
- [3] H. Yang, H. Pang, Z. Qiang, Z. Ma, and W. Zhou, "Surface-normal Fano filters based on transferred silicon nanomembranes on glass substrates," *Electronics Letters*, vol. 44, pp. 858-859, 2008.
- [4] Z. Qiang, H. Yang, L. Chen, H. Pang, Z. Ma, and W. Zhou, "Fano filters based on transferred silicon nanomembranes on plastic substrates," *Applied Physics Letters*, vol. 93, pp. 061106-3, 2008.
- [5] L. Chen, Z. Qiang, H. Yang, H. Pang, Z. Ma, and W. Zhou, "Polarization and angular dependent transmissions on transferred nanomembrane Fano filters," *Opt. Express*, vol. 17, pp. 8396-8406, 2009.
- [6] L. Chen, H. Yang, Z. Qiang, H. Pang, L. Sun, Z. Ma, R. Pate, A. Stiff-Roberts, S. Gao, J. Xu, G. J. Brown, and W. Zhou, "Colloidal quantum dot absorption enhancement in flexible Fano filters," *Applied Physics Letters*, vol. 96, pp. 083111-3, 2010.
- [7] W. Yang, H. Yang, G. Qin, Z. Ma, J. Berggren, M. Hammar, R. Soref, and W. Zhou, "Large-area InP-based crystalline nanomembrane flexible photodetectors," *Applied Physics Letters*, vol. 96, pp. 121107-3, 2010.
- [8] H. Yang, S. Chuwongin, Z. Qiang, L. Chen, H. Pang, Z. Ma, and W. Zhou, "Resonance control of membrane reflectors with effective index engineering," *Applied Physics Letters*, vol. 95, pp. 023110-3, 2009.
- [9] D. Taillaert, W. Bogaerts, P. Bienstman, T. F. Krauss, P. Van Daele, I. Moerman, S. Verstuyft, K. De Mesel, and R. Baets, "An out-of-plane grating coupler for efficient butt-coupling between compact planar waveguides and single-mode fibers," *Quantum Electronics, IEEE Journal of*, vol. 38, pp. 949-955, 2002.
- [10] F. Van Laere, G. Roelkens, M. Ayre, J. Schrauwen, D. Taillaert, D. Van Thourhout, T. F. Krauss, and R. Baets, "Compact and Highly Efficient Grating Couplers Between Optical Fiber and Nanophotonic Waveguides," *Lightwave Technology, Journal of*, vol. 25, pp. 151-156, 2007.
- [11] D. Taillaert, F. Van Laere, M. Ayre, W. Bogaerts, D. Van Thourhout, P. Bienstman, and R. Baets, "Grating couplers for coupling between optical fibers and nanophotonic waveguides," *Japanese Journal of Applied Physics Part 1-Regular Papers Brief Communications & Review Papers*, vol. 45, pp. 6071-6077, 2006.

- [12] D. Taillaert, P. Bienstman, and R. Baets, "Compact efficient broadband grating coupler for silicon-on-insulator waveguides," *Opt. Lett.*, vol. 29, pp. 2749-2751, 2004.
- [13] R. T. Chen, L. Lei, C. Chulchae, Y. J. Liu, B. Bihari, L. Wu, S. Tang, R. Wickman, B. Picor, M. K. Hibb-Brenner, J. Bristow, and Y. S. Liu, "Fully embedded board-level guided-wave optoelectronic interconnects," *Proceedings of the IEEE*, vol. 88, pp. 780-793, 2000.
- [14] T. Dillon, J. Murakowski, S. Shi, and D. Prather, "Fiber-to-waveguide coupler based on the parabolic reflector," *Opt. Lett.*, vol. 33, pp. 896-898, 2008.
- [15] B. Wang, J. Jiang, and G. Nordin, "Compact slanted grating couplers," *Opt. Express*, vol. 12, pp. 3313-3326, 2004.
- [16] W. Bin, J. Jianhua, and G. P. Nordin, "Embedded slanted grating for vertical coupling between fibers and silicon-on-insulator planar waveguides," *Photonics Technology Letters, IEEE*, vol. 17, pp. 1884-1886, 2005.
- [17] L. Frederik Van, V. K. Maria, T. Dirk, T. Dries Van, F. K. Thomas, and B. Roel, "Compact Slanted Grating Couplers Between Optical Fiber and InP&ndash;InGaAsP Waveguides," *Photonics Technology Letters, IEEE*, vol. 19, pp. 396-398, 2007.
- [18] J. Schrauwen, F. Van Laere, D. Van Thourhout, and R. Baets, "Focused-Ion-Beam Fabrication of Slanted Grating Couplers in Silicon-on-Insulator Waveguides," *Photonics Technology Letters, IEEE*, vol. 19, pp. 816-818, 2007.
- [19] G. Roelkens, D. Vermeulen, D. Van Thourhout, R. Baets, S. Brisson, P. Lyan, P. Gautier, and J. M. Fedeli, "High efficiency diffractive grating couplers for interfacing a single mode optical fiber with a nanophotonic silicon-on-insulator waveguide circuit," *Applied Physics Letters*, vol. 92, pp. 131101-3, 2008.
- [20] G. Roelkens, D. Van Thourhout, and R. Baets, "High efficiency Silicon-on-Insulator grating coupler based on a poly-Silicon overlay," *Opt. Express*, vol. 14, pp. 11622-11630, 2006.
- [21] P. Bienstman and R. Baets, "Optical modelling of photonic crystals and VCSELs using eigenmode expansion and perfectly matched layers," *Optical and Quantum Electronics*, vol. 33, pp. 327-341, 2001.
- [22] P. Bienstman and R. Baets, "Rigorous and efficient optical VCSEL model based on vectorial eigenmode expansion and perfectly matched layers," *Optoelectronics, IEE Proceedings -*, vol. 149, pp. 161-165, 2002.
- [23] C. Vassallo, *Optical waveguide concepts*. Amsterdam [etc.]: Elsevier, 1991.
- [24] D. Taillaert, C. Harold, P. I. Borel, L. H. Frandsen, R. M. D. L. Rue, and R. Baets, "A compact two-dimensional grating coupler used as a polarization splitter," *Photonics Technology Letters, IEEE*, vol. 15, pp. 1249-1251, 2003.
- [25] M. Notomi, A. Shinya, S. Mitsugi, E. Kuramochi, and H. Ryu, "Waveguides, resonators and their coupled elements in photonic crystal slabs," *Opt. Express*, vol. 12, pp. 1551-1561, 2004.

- [26] S. Scheerlinck, J. Schrauwen, G. Roelkens, D. Van Thourhout, and R. Baets, "Vertical fiber-to-waveguide coupling using adapted fibers with an angled facet fabricated by a simple molding technique," *Appl. Opt.*, vol. 47, pp. 3241-3245, 2008.
- [27] G. Roelkens, D. V. Thourhout, and R. Baets, "High efficiency grating coupler between silicon-on-insulator waveguides and perfectly vertical optical fibers," *Opt. Lett.*, vol. 32, pp. 1495-1497, 2007.
- [28] S. S. Wang, R. Magnusson, J. S. Bagby, and M. G. Moharam, "Guided-mode resonances in planar dielectric-layer diffraction gratings," *J. Opt. Soc. Am. A*, vol. 7, pp. 1470-1474, 1990.
- [29] M. C. Y. Huang, Y. Zhou, and C. J. Chang-Hasnain, "A surface-emitting laser incorporating a high-index-contrast subwavelength grating," *Nat Photon*, vol. 1, pp. 119-122, 2007.
- [30] S. Fan and J. D. Joannopoulos, "Analysis of guided resonances in photonic crystal slabs," *Physical Review B*, vol. 65, p. 235112, 2002.
- [31] R. Magnusson and S. S. Wang, "New principle for optical filters," *Applied Physics Letters*, vol. 61, pp. 1022-1024, 1992.
- [32] K. Umetsu, R. Furutnani, S. Osawa, T. Takatsuji, and T. Kurosawa, "Geometric calibration of a coordinate measuring machine using a laser tracking system," *Measurement Science & Technology*, vol. 16, pp. 2466-2472, 2005.
- [33] H. Jiang, S. Osawa, T. Takatsuji, H. Noguchi, and T. Kurosawa, "High-performance laser tracker using an articulating mirror for the calibration of coordinate measuring machine," *Optical Engineering*, vol. 41, pp. 632-637, 2002.
- [34] C. R. Cooke, "Automatic Laser Tracking and Ranging System," *Appl. Opt.*, vol. 11, pp. 277-284, 1972.
- [35] O. Nakamura, M. Goto, K. Toyoda, N. Takai, T. Kurosawa, and T. Nakamata, "A laser tracking robot-performance calibration system using ball-seated bearing mechanisms and a spherically shaped cat's-eye retroreflector," *Review of Scientific Instruments*, vol. 65, pp. 1006-1011, 1994.
- [36] I. Hahn, M. Weilert, X. Wang, and R. Goullioud, "A heterodyne interferometer for angle metrology," *Review of Scientific Instruments*, vol. 81, pp. 045103-6, 2010.
- [37] M. Toyoda, K. Araki, and Y. Suzuki, "Wave-Front Tilt Sensor with Two Quadrant Detectors and its Application to a Laser Beam Pointing System," *Appl. Opt.*, vol. 41, pp. 2219-2223, 2002.
- [38] S. Schlamminger, K. Y. Choi, T. A. Wagner, J. H. Gundlach, and E. G. Adelberger, "Test of the Equivalence Principle Using a Rotating Torsion Balance," *Physical Review Letters*, vol. 100, p. 041101, 2008.
- [39] P. A. Forrester and K. F. Hulme, "LASER RANGEFINDERS," *Optical and Quantum Electronics*, vol. 13, pp. 259-293, 1981.

- [40] K. Mawatari and K. Shimoide, "Reflective thermal lens detection device," *Lab on a Chip*, vol. 6, pp. 127-130, 2006.
- [41] L. M. Manojlovic and Z. P. Barbaric, "Optimization of Optical Receiver Parameters for Pulsed Laser-Tracking Systems," *Instrumentation and Measurement, IEEE Transactions on*, vol. 58, pp. 681-690, 2009.
- [42] M. Toyoda, K. Araki, and Y. Suzuki, "Measurement of the characteristics of a quadrant avalanche photodiode and its application to a laser tracking system," *Optical Engineering*, vol. 41, pp. 145-149, 2002.
- [43] Z. Zhang, Q. Feng, Z. Gao, C. Kuang, C. Fei, Z. Li, and J. Ding, "A new laser displacement sensor based on triangulation for gauge real-time measurement," *Optics and Laser Technology*, vol. 40, pp. 252-255, 2008.
- [44] H. Müller, S.-w. Chiow, Q. Long, C. Vo, and S. Chu, "Active sub-Rayleigh alignment of parallel or antiparallel laser beams," *Opt. Lett.*, vol. 30, pp. 3323-3325, 2005.
- [45] G. Giuliani, S. Donati, M. Passerini, and T. Bosch, "Angle measurement by injection detection in a laser diode," *Optical Engineering*, vol. 40, pp. 95-99, 2001.
- [46] T. Fujita, K. Nakamura, and T. Matozaki, "Simple and Accurate Propagation-Angle Observation of a Collimated Laser Beam within a Short Optical Path Range by Use of a Dual-Focus Fresnel Lens," *Optical Review*, vol. 12, pp. 260-263-263, 2005.
- [47] A. Makynen, J. T. Kostamovaara, and R. A. Myllyla, "Displacement sensing resolution of position-sensitive detectors in atmospheric turbulence using retroreflected beam," *Instrumentation and Measurement, IEEE Transactions on*, vol. 46, pp. 1133-1136, 1997.
- [48] A. Tuantranont, V. M. Bright, J. Zhang, W. Zhang, J. A. Neff, and Y. C. Lee, "Optical beam steering using MEMS-controllable microlens array," *Sensors and Actuators a-Physical*, vol. 91, pp. 363-372, 2001.
- [49] D. A. May-Arrioja, N. Bickel, and P. LiKamWa, "Optical beam steering using InGaAsP multiple quantum wells," *Photonics Technology Letters, IEEE*, vol. 17, pp. 333-335, 2005.
- [50] M. Jarrahi, R. Fabian, W. Pease, D. A. B. Miller, and T. H. Lee, "High-speed optical beam-steering based on phase-arrayed waveguides," *Journal of Vacuum Science & Technology B*, vol. 26, pp. 2124-2126, 2008.
- [51] A. Hosseini, D. Kwong, Z. Yang, C. Yun-Sheng, F. Crnogorac, R. F. W. Pease, and R. T. Chen, "Unequally Spaced Waveguide Arrays for Silicon Nanomembrane-Based Efficient Large Angle Optical Beam Steering," *Selected Topics in Quantum Electronics, IEEE Journal of*, vol. 15, pp. 1439-1446, 2009.
- [52] D. R. Scifres, W. Streifer, and R. D. Burnham, "Beam scanning with twin-stripe injection lasers," *Applied Physics Letters*, vol. 33, pp. 702-704, 1978.
- [53] S. Mukai, M. Watanabe, H. Itoh, H. Yajima, Y. Hosoi, and S. Uekusa, "BEAM SCANNING AND SWITCHING CHARACTERISTICS OF TWIN-STRIPED LASERS WITH A REDUCED STRIPE SPACING," *Optical and Quantum Electronics*, vol. 17, pp. 431-434, 1985.

- [54] T. Ide, M. Shimizu, S. Mukai, M. Ogura, T. Kikuchi, Y. Suzuki, R. Kaji, H. Itoh, M. Watanabe, H. Yajima, and T. Nemoto, "Continuous output beam steering in vertical-cavity surface-emitting lasers with two p-type electrodes by controlling injection current profile," *Japanese Journal of Applied Physics Part 1-Regular Papers Short Notes & Review Papers*, vol. 38, pp. 1966-1970, 1999.
- [55] Y. Kurosaka, S. Iwahashi, Y. Liang, K. Sakai, E. Miyai, W. Kunishi, D. Ohnishi, and S. Noda, "On-chip beam-steering photonic-crystal lasers," *Nat Photon*, vol. 4, pp. 447-450, 2010.
- [56] H. Kosaka, T. Kawashima, A. Tomita, M. Notomi, T. Tamamura, T. Sato, and S. Kawakami, "Photonic crystals for micro lightwave circuits using wavelength-dependent angular beam steering," *Applied Physics Letters*, vol. 74, pp. 1370-1372, 1999.
- [57] L. Vivien, D. Pascal, S. Lardenois, D. Marris-Morini, E. Cassan, F. Grillot, S. Laval, J.-M. Fédéli, and L. El Melhaoui, "Light Injection in SOI Microwaveguides Using High-Efficiency Grating Couplers," *J. Lightwave Technol.*, vol. 24, pp. 3810-3815, 2006.
- [58] C. J. Chen, K. K. Choi, L. Rokhinson, W. H. Chang, and D. C. Tsui, "Corrugated quantum well infrared photodetectors for polarization detection," *Applied Physics Letters*, vol. 74, pp. 862-864, 1999.
- [59] S. Ura, H. Sunagawa, T. Suhara, and H. Nishihara, "Focusing grating couplers for polarization detection," *Lightwave Technology, Journal of*, vol. 6, pp. 1028-1033, 1988.
- [60] T. Yongbo, D. Daoxin, and H. Sailing, "Proposal for a Grating Waveguide Serving as Both a Polarization Splitter and an Efficient Coupler for Silicon-on-Insulator Nanophotonic Circuits," *Photonics Technology Letters, IEEE*, vol. 21, pp. 242-244, 2009.
- [61] N. J. Bridge and A. D. Buckingham, "The Polarization of Laser Light Scattered by Gases," *Proceedings of the Royal Society of London. Series A, Mathematical and Physical Sciences*, vol. 295, 334-349, 1966.
- [62] C. Wieman and T. W. Hänsch, "Doppler-Free Laser Polarization Spectroscopy," *Physical Review Letters*, vol. 36, p 1170-1173, (1976).

## BIOGRAPHICAL INFORMATION

Tapas Kumar Saha has received the B.E. Degree from Bengal Engineering and Science University, Shibpur in 2005, M.E. Degree from Jadavpur University in 2007 and PhD from University of Texas at Arlington in 2012. His research area include design, fabrication and characterization of optoelectronics and nanophotonics devices.